NASA TECHNICAL MEMORANDUM

NASA TM X-73413

NASA TM X-73413

EXPERIMENTAL AND THEORETICAL INVESTIGATION OF FATIGUE LIFE IN REUSABLE ROCKET THRUST CHAMBERS

by Ned P. Hannum, Harold J. Kasper, and Albert J. Pavli
Lewis Research Center
Cleveland, Ohio 44135

TECHNICAL PAPER to be presented at
the Twelfth Propulsion Conference
sponsored by the American Institute of Aeronautics and Astronautics and the Society of Automotive Engineers
Palo Alto, California, July 26-28, 1976

EXPERIMENTAL AND THEORETICAL INVESTIGATION OF FATIGUE LIFE IN REUSABLE ROCKET THRUST CHAMBERS

Ned P. Hannum, Harold J. Kasper, and Albert J. Pavli
Lewis Research Center
National Aeronautics and Space Administration
Cleveland, Ohio 44135

Summary

During a test program to investigate low-cycle thermal fatigue, 13 rocket combustion chambers were fabricated and cyclically test fired to failure. Six oxygen-free, high-conductivity (OFHC) copper and seven Amzirc chambers were tested. The chamber liners were fabricated of copper or copper alloy and contained milled coolant channels. The chambers were completed by means of an electroformed nickel closeout. The combustion chamber pressures were 4.16 and 5.52 MN/m^2 (600 and 800 psia). The oxidant-fuel ratio for the liquid oxygen and gaseous hydrogen propellants was 6.0. The failures in the OFHC copper chambers were not typical fatigue failures but are described as creep rupture enhanced by ratcheting. The coolant channels bulged toward the chamber centerline, resulting in progressive thinning of the wall during each cycle. The failures in the Amzirc alloy chambers were caused by low-cycle thermal fatigue. The lives were much shorter than were predicted by an analytical structural analysis computer program used in conjunction with fatigue life data from isothermal test specimens. The reason for this discrepancy was that the zirconium in the alloy was not evenly distributed in the chamber material as it had been in the test specimens. Consequently, the life that was achieved was nominally the same as would have been predicted from OFHC copper isothermal test data.

Introduction

The requirement for reusability of high-chamber-pressure, regeneratively cooled, rocket thrust chambers in the near future has precipitated experimental and analytical low-cycle thermal fatigue studies with high-conductivity materials. High-thermal-conductivity materials are required for the thrust chamber liners. The heat flux associated with the high chamber pressures (13.8 to 20.7 MN/m^2 (2000 to 3000 psia)) of proposed high-performance engines for future space transportation systems cannot be accommodated by the lower conductivity materials at thicknesses necessary for the pressure loads. The expected design life for these future reusable thrust chambers is from 100 to 300 cycles. The work reported herein was not intended to demonstrate a particular life goal but rather to produce several low-cycle thermal fatigue failures in rocket thrust chambers for the purpose of enhancing our knowledge of such failures and improving the present capabilities in low-cycle thermal fatigue analysis and life prediction.

In 1967 and 1968 a high-chamber-pressure program to evaluate the technology for milled-channel copper thrust chambers was conducted jointly by Boelkow GmbH and Rocketdyne, a division of North American Rockwell Corporation[1,2]. During testing at chamber pressures from 13.8 to 20.7 MN/m^2 (2000 to 3000 psia) fatigue cracks appeared in the throat of one of the oxygen-free, high-conductivity (OFHC) copper chambers. It was not within the scope of that work to investigate low-cycle thermal fatigue, but it was identified as a problem area for high-pressure, reusable rocket chambers.

In 1972, low-cycle thermal fatigue tests were conducted by the U.S. Air Force on rocket combustion chambers that had been designed and fabricated by Rocketdyne[3,4]. These tests were conducted at a chamber pressure of 5.2 MN/m^2 (750 psia). Experimentally obtained fatigue life was compared with the analytical predictions for two zirconium-copper alloys: Amzirc, which was obtained from American Metals Climax, Inc; and Narloy-Z, which was obtained from Rocketdyne.

The NASA Manned Space Flight Center later acquired more of these chambers and continued the work. The life analysis for these tests is reported in reference 5.

In the previous work the nature of the thermal fatigue problem in rocket combustors was defined only for a few select configurations. The questions still unanswered were how fatigue life was affected by such variables as chamber contour, material, chamber pressure, wall temperature, and start cycle. Further, the ability of analysis to predict fatigue life and the consistency of experimental results were also not determined. It was in response to these problems that the present work was undertaken. It presents a comprehensive investigation into the effects of two chamber contours, three chamber materials, two chamber pressures, two wall temperatures (two coolant flows), and two start cycles on fatigue life. This is done with 13 separate combustion chambers of which 4 are duplicate configurations for repeatability considerations.

The combustion chambers had a throat diameter of 6.60 cm (2.60 in.) and were fabricated and cyclically tested to failure with hydrogen and oxygen propellants. The combustion chamber pressures used in the present work were 4.14 and 5.52 MN/m^2 (600 to 800 psia). The fabrication method used was electroform closeout of milled coolant passages, which is typical of high-pressure, high-performance rocket engines, such as the Space Shuttle Main Engine (SSME). Attempts were made to correlate the experimentally determined life with analytical predictions for each of the 13 chambers used. The analytical capabilities required to make life predictions included a thermal analyzer program, SINDA[6], and a structural finite element program, RETSCP[7]. The structural analysis included combined thermal and pressure loading. Comprehensive isothermal strength and fatigue data were obtained for several candidate thrust-chamber-liner materials. These data are reported in references 8 and 9 and include material properties and fatigue data for the three chamber liners used in the present testing: OFHC copper, annealed Amzirc, and half-hard Amzirc.

After the structural analysis was completed, the effective strain-range data were applied to the reference isothermal fatigue data in order to produce a predicted life for each of the 13 chambers tested. These predicted and measured results were then compared. In addition, destructive tests were

made on representative fatigued chambers to determine the metallurgical characteristics of the liner materials near the fatigued areas for comparison with the reference materials. Also crack propagation and liner deformation were investigated by destructive means.

Apparatus

Test Facility

The investigation was conducted at the Lewis Research Center rocket engine test facility. This is a 222,410-newton (50,000-lbf), sea-level rocket test stand equipped with an exhaust-gas muffler and scrubber. The facility used pressurized propellant-storage tanks to supply the propellants to the combustor. Propellants were liquid oxygen and ambient-temperature gaseous hydrogen. Liquid hydrogen was used as the coolant. Details of the installation are shown in Figures 1(a) and (b).

Figure 1(a) shows the thrust stand and exhaust-gas scrubber entrance with a typical combustion chamber mounted in place. Figure 1(b) is a schematic of the test facility showing the propellant supply and the instrumentation locations. The separate coolant flow circuit allows coolant flow to be independent of engine propellant flow. The spent hydrogen coolant was disposed of through a burn stack. For test convenience an external ignitor torch was used to ignite the propellants. At ignition the flame front would pass upward through the throat and ignite the propellants in the combustion chamber.

Injectors

With the injectors used in this investigation, the fuel (gaseous hydrogen) was injected through a porous Rigimesh face plate. The oxidant was injected through 85 showerhead tubes distributed evenly over the injector face. Figure 2(a) shows the face side of an injector; Figure 2(b) is a cross-sectional sketch of one element, showing the liquid oxygen tube and the porous face through which the fuel was injected. At the start of this program, this injector design was selected from several other candidate designs because of its excellent performance, heat flux uniformity, and durability characteristics. The heat flux uniformity of the candidate injectors was compared by conducting firing tests with ablative chambers and examining the erosion patterns. The selected injector was the best in heat flux uniformity and durability and had an energy release efficiency of 97.5%, with all data within a band of $\pm$0.5%. The performance procedure used to compute injector efficiency is outlined in reference 10.

During the performance testing with the heat-sink thrust chambers, tests were made with high-response piezoelectric pressure transducers to measure combustion chamber pressure oscillations and thereby to ascertain whether combustion instability was present. No instability was found.

Fatigue Combustion Chambers

The details of the thrust chambers used in the low-cycle fatigue life investigation are shown in Figures 3(a) to (f). The chambers were made in two contours, contour A and contour B (Fig. 3(a)). The chambers, which had a contraction ratio of 3.70, were 38.1 cm (15 in.) long overall with the throat located 25.4 cm (10 in.) from the injector face. The throat was 6.60 cm (2.6 in.) in diameter, and the nozzle exit was 13.2 cm (5.2 in.) in diameter. The chamber liners were made of copper or copper alloy and had coolant passages machined into the outer surface (Fig. 3(b)). Three materials were used for the liners: oxygen-free, high-conductivity (OFHC) copper; annealed Amzirc, which is an American Metal Climax, Inc., 0.15% zirconium-copper alloy; and Amzirc in a half-hard state that was achieved by a cold spinning operation prior to final machining. After machining, the coolant passages were temporarily filled with a wax, and a layer of nickel was electrodeposited onto the outer surface to form the nickel outer jacket shown in Figure 3(c). The coolant passage cross section thus formed is shown in Figure 3(d), which is a section through the throat plane of the chamber. The coolant passage dimensions were selected to provide a hot-gas-side wall temperature of 811 K (1460° R) in the throat for the operating conditions of 4.14-MN/m^2 (600-psia) chamber pressure and 0.91-kg/sec (2.0-lb/sec) coolant flow rate. Much lower temperatures were selected for other areas of the chamber to insure that the throat would be the region of highest strain. All 13 chambers used in the testing were designed with the same coolant passage height at the throat section. After electroforming, the wax was melted out of the coolant passages, the manifolds welded on, and the instrumentation attached. Figures 3(e) and (f) show two such completed chambers, one of each contour.

The instrumentation on the thrust chambers consisted primarily of two types of thermocouples. Copper/constantan alloy thermocouples were spot welded onto the outside diameter (O.D.) of the combustion chamber. High-response Chromel/constantan thermocouples were placed inside a 0.35-mm (0.014-in.) stainless steel sheath and were spring loaded against the bottom of a hole drilled into the copper rib. The thermocouple tip was located within 1.27 mm (0.050 in.) of the hot-gas-side wall surface (chamber inside diameter (I.D.)). A typical rib thermocouple hole is shown in Figure 3(d). Inspection of the precision-machined holes indicated that the distance from bottom of the hole to the I.D. was 1.27$\pm$0.05 mm (0.050$\pm$0.002 in.). Analysis has shown that the temperature profile across the rib at this radial station is essentially flat, and precision in circumferential location of the thermocouple hole is necessary only to keep from breaking into a coolant passage. To make sure that the thermocouple holes did not break into the coolant passages, each was leak tested with helium. During the course of this program, considerable development work was done in perfecting the temperature measurement technique in these rib holes. As a result, temperature data for some of the early chambers were not accurate. In the analysis of these chambers, it was assumed that chambers that were fabricated from the same material and tested at the same conditions operated at the same wall temperature. The final version of the rib thermocouple was a sheath of 0.35-mm (0.014-in.) stainless-steel tubing in which 0.025-mm (0.001-in.) diameter Chromel and constantan wires made a junction at the end of the tube in a small "bullet"-shaped tip of silver solder. The probe tip was then gold plated with a thickness of approximately 0.005 mm (0.0002 in.) in order to provide a malleable contact surface to press against the copper bottom of the hole in the rib. The probe was then spring

loaded against the hole bottom with a force of approximately 120 g (0.26 lb).

During the course of the program a source of error was recognized in trying to measure the rib temperature. The outside surface of the chamber would cycle from below 55 K (100° R) between firings to above 222 K (400° R) while firing. The thermocouple holes would cryopump condensable gases, which would then evaporate from the holes during each cycle. The temperature reading was thus being affected by both the heat of condensation (and evaporation) of these condensable gases and by the presence of surface corrosion that formed as a result of the environment. To avoid this problem, a flow of low-pressure (17.2 kN/m^2; 2.5 psig) gaseous helium was used to effectively displace any condensable gases from the entrance to the thermocouple holes.

Procedure

Two test cycles were used in this program. They are shown in Figure 4. The first was a slow test cycle that attempted to bring the wall temperatures up so that the maximum temperature difference between the hot-gas-side wall and the chamber O.D. would occur during steady-state operation. The time of maximum temperature difference usually produces the maximum strain. Temperatures would be relatively easy to measure at steady-state conditions, and therefore the cycle would be well characterized. In practice, however, the maximum temperature difference did not occur at steady-state conditions in spite of the slow ramp start. Instead it occurred during the start ramp and was 25 to 30% greater than steady-state values. It was impractical to consider extending the ramp duration, especially for a cyclic test program, since the time and propellant expended for testing would be excessive. For these reasons, a second test cycle, referred to as "the fast cycle" (Fig. 4), was developed. In this cycle the maximum temperature difference would occur during the sudden start transient. With the fast cycle, the combustion chamber reached full chamber pressure in 0.05 to 0.06 sec, and the maximum temperature difference across the wall was equal to approximately 130% of the steady-state value. Once the cycle was well beyond the time when the maximum temperature difference had occurred, which was approximately 0.30 sec after start, the chamber was shut down. This gave a rated thrust duration of about 0.85 sec. The liquid hydrogen coolant flow was continued during a 1.4-sec shutdown, which was enough time to cool all parts of the chamber to original conditions. Then the chamber was recycled. This gave a total cycle duration of 2.3 sec. With the storage capability of the facility, as many as 125 cycles could be made in a single firing series. Accurate temperature measurement on the chamber was very important in order to characterize the thermal gradients necessary to make the life analysis and predictions. With the fast cycle, thermocouples with a fast response were needed, especially in the rib holes. To fill this need, the rib thermocouple probe described in the section Apparatus was developed.

The test cycles were programmed into a solid-state timer that was accurate and repeatable to within ±0.001 sec. Fuel and oxidizer flows were controlled by fixed-position valves and propellant tank pressures. Coolant flow was controlled by a cavitating venturi. Coolant inlet pressure was controlled by coolant tank pressure, and coolant exit pressure was kept constant by a closed-loop controller modulating a backpressure valve. Control room operation of the test included monitoring of the test hardware by means of three closed-circuit television cameras and one cell microphone. The output of the microphone and one television camera were recorded on magnetic tape for later playback. The cell microphone was the primary data sensor for determining the time of the fatigue failure. During the cooldown phase of the cycle, between thrust pulses while the coolant continued flowing, any coolant leak significant enough to indicate a throughcrack could be heard very clearly. In most cases it was possible to recognize a failure and to stop the cyclic testing within two cycles of the failure. In playing back the audio tape, we could precisely determine the exact cycle when failure occurred in all but two chambers, which are discussed in the following section.

Test Results

Test Conditions

Thirteen rocket chambers were thermally cycled to failure. Eight of these chambers were tested with the same test cycle and under the same test conditions. The test matrix giving the test conditions, the chamber numbers, the chamber liner materials, and the chamber contours is shown in Table I. Six of the rocket chamber liners were made of oxygen-free, high conductivity (OFHC) copper. The three B contour chambers were in this group. Four chamber liners were made of Amzirc in a fully annealed condition, and three were fabricated from Amzirc that had been cold worked to a half-hard condition by spinning.

The baseline cycle used for eight of the chambers in the test matrix was the fast cycle described in Figure 4, with a combustion chamber pressure of 4.14 MN/m^2 (600 psia) and a coolant flow rate of 0.91 kg/sec (2.0 lb/sec). Two of each type of chamber were tested in this manner (Table I). Two other chambers were tested with the coolant flow rate reduced to 0.59 kg/sec (1.3 lb/sec). Another two chambers were tested with a coolant flow rate of 0.59 kg/sec (1.3 lb/sec) but with the chamber pressure increased to 5.52 MN/m^2 (800 psia). One chamber was tested under the baseline conditions of 4.14-MN/m^2 (600 psia) chamber pressure and 0.91-kg/sec (2.0 lb/sec) coolant flow rate but with the slow cycle described in Figure 4.

Care was taken to insure that the flow rates and fluid pressures were nearly the same for each cycle of a test series. Combustion oxidant-fuel ratio was nominally 6.0, with a range of approximately ±0.15. Combustion chamber pressure varied ±3% from the nominal value stated for each cycle. Coolant flow rate varied ±2% from the nominal value stated for each cycle. The effect on fatigue life of test-condition variations of this order was assumed to be well within the accuracy of the life predictions. Cycle-by-cycle data for these and other pressure and flow rate parameters are not presented.

Of the 13 chambers fabricated and tested, eight were instrumented to measure the temperature in the coolant ribs at a point 1.27 mm (0.050 in.) from the hot-gas-side wall and in the plane of the throat. Four spring-loaded thermocouples (described in the section Apparatus) were located 90° apart. For each

rib thermocouple a corresponding thermocouple was peened onto the chamber O.D.

Typical rib temperature data for a single cycle are presented in Figure 5. These data are for the baseline fast cycle, where combustion chamber pressure was 4.14 MN/m^2 (600 psia) and the coolant flow rate was 0.91 kg/sec (2.0 lb/sec). The data presented are for the twenty-sixth cycle with chamber S/N 70 but are typical of all chambers in terms of transient response and the range of data between the four thermocouples. The figure shows that the difference in temperature between the hottest and the coldest circumferential locations was approximately 69 K (125° R) at the end of the transient and less than that toward the end of the firing. For the fast cycle (Fig. 4) the rise time for the chamber pressure transient was approximately 50 msec. The rib temperature transient occurred in approximately 0.4 sec. Also shown in Figure 5 are typical chamber O.D. temperature data as a function of time for one firing cycle. It can be seen that this parameter does not come to steady state during a firing when the fast cycle is used.

Figures 6(a) and (b) summarize the data recorded during the last 0.1 second of each firing for each cycle during the life of chamber S/N 101. The data taken at the hottest rib station and at the corresponding chamber O.D. temperature station are presented in Figure 6(a). The coolant temperature rise data are presented in Figure 6(b). For all but one of the seven chambers where rib temperature measurements were taken during each cycle of chamber life, there was a trend of increasing rib temperature, chamber O.D. temperature, and coolant temperature rise from the first cycles to the last cycles. The amount of this increase seemed to be related to the amount of deformation that occurred because of the different-strength liner materials tested. The one instrumented chamber that did not show this trend of increasing temperature with life was half-hard Amzirc chamber S/N 121. The rib temperature for this chamber remained constant with each succeeding cycle. The coolant passage deformation was also considerably less for half-hard Amzirc chambers than for the other chambers.

To determine experimentally the effect of coolant flow rate on measured rib temperature, the flow rate was varied slightly during the first six cycles with chamber S/N 101. These data are presented in Figure 6(c). From the slope of these data it can be seen that a ±2% variation in coolant flow rate is equivalent to a ±11 K (±20° R) variation in rib temperature. The effect of the nonstandard coolant flow rate on rib temperature, chamber O.D. temperature, and coolant temperature rise during the first six cycles of testing can also be seen in Figures 6(a) and (b).

The experimental data for each test chamber are presented in Table II. The cycle type refers to the two cycles described in Figure 4. Experimental steady-state rib temperature data from the hottest thermocouple location are presented for two different times during the life of each chamber. These two temperatures, referred to as "new" and "end," are averages of the first few cycles when the chamber is new and of the last few cycles just before fatigue failure. Where no rib temperature data are indicated, either the chamber was not instrumented or, in the case of chamber S/N 50, the data for early test cycles were not considered to be valid because of the instrumentation methods used. Chamber S/N 50 was reinstrumented for the last few test cycles. Although some chambers were not instrumented to measure rib temperature, all fluid pressures, flow rates, and combustion performance parameters were measured for all tests to insure the proper test conditions.

Experimental Cycles to Failure

For this investigation, a fatigue failure was defined as a chamber liner inner-wall throughcrack that permitted audible detection of a coolant leak into the combustion chamber. In practice, cracks of approximately 1000 μm in length (nominally 1 wall thickness) are the minimum size detectable by this method. The cycle during which the flaw became a throughcrack was determinable by the method described in the section Procedure and is listed for each chamber in Table II under experimental cycles to failure.

Most tests were manually aborted within one or two cycles after it was suspected that a failure had occurred. The coolant passages were then pressure checked to determine the number and location(s) of the failures. There is no uncertainty about the experimental cycles to failure tabulated in Table II for any of the chambers tested, except chambers S/N 90 and S/N 100, which are both annealed Amzirc. For all the other chambers there was only one failure site initially, and the failure cycle was easily determined from listening to the audio tapes. Some typical failure sites are shown in Figure 7. With the OFHC chamber liners there was significant bulging of the channels out into the combustion chamber. Figure 7(a) shows the throat section of an OFHC copper chamber in profile; the bulging can be seen, as well as the failure site. The failure site is visible both on the liner and reflected in a mirror. The crack is approximately 2 mm (0.08 in.) long and is located near the center of one of the bulges. Figure 7(b) shows a failure site in a half-hard Amzirc chamber. There is much less bulging and the crack is approximately 8 mm (0.31 in.) long.

Three of the failed chambers were retested with new rib temperature instrumentation to confirm the measurements. During these retests, additional damage occurred. Those chambers retested, the number of additional cycles, and the additional damage are noted in the remarks column of Table II. Annealed Amzirc chamber 80 was retested for an additional 10 cycles. During those 10 cycles the crack grew from approximately 6 mm to approximately 19 mm (0.24 in. to 0.75 in.). The crack is shown two cycles after the initial failure and then 12 cycles after the initial failure in Figures 7(c) and (d), respectively. Similarly the fatigue crack in chamber S/N 90 grew from 7 mm to 15 mm (0.28 in. to 0.59 in.) during eight retest cycles. During 13 retest cycles with OFHC copper chamber S/N 50, three additional pinhole failures occurred in the throat region. These failures look much like the crack except that they are bulges not linear cracks.

As already mentioned it was not possible to precisely determine the failure cycle for two of the chambers. The reason was that, after a significant failure was detected by the change in sound and the testing was aborted, additional small failure sites were also located. Table II indicates that with chamber S/N 100 there were two pinhole leaks in the throat region in addition to the fa-

tigue crack. These pin holes are shown in Figure 7(e). Similarly, with chamber S/N 90 there were three pinhole leaks in addition to the fatigue crack. In both cases the number of experimental cycles to failure reported in Table II is thought to reflect the cycle when the larger fatigue crack occurred because the change in sound produced from that size leak was clearly audible.

Although the rib temperature data are included and are considered to be typical, the cycles-to-failure data for chamber S/N 101 are not included in Table II because the failure occurred at a nontypical wall temperature. Prior to cyclic testing of chamber S/N 101, a small leak through the liner was detected near the injector end. The leak was repaired by using a light surface braze. Because the subsequent fatigue crack was in line with this repair, the chamber was sectioned and it was determined that two adjacent coolant passages were partially blocked by the braze material. The nearest rib temperature measurements were four ribs away; consequently, there were no experimental temperature data for use in the life analysis. The fatigue failure occurred during cycle 51. Seven of the 13 chambers have been inspected by destructive means. There is no evidence or suspicion that any other passages in any other chambers were blocked.

From the cycles to failure in Table II, it can be seen that the four OFHC chambers (S/N's 40, 50, 70, and 71) tested with the fast cycle at 4.14-MN/m^2 (600-psia) chamber pressure and 0.91-kg/sec (2.0-lb/sec) coolant flow rate all failed between 130 and 165 cycles. Further, for the present case, when the design was for the same hot-gas-side wall temperature, there was no effect of chamber contour on fatigue life (chambers S/N 40 and S/N 50 were contour B; chambers S/N 70 and 71 were contour A). The OFHC copper chambers S/N 10 and S/N 60 failed much earlier than did these. Chamber S/N 10 was fabricated from a billet containing very large columnar grains. The other chambers had a much smaller grain size, and it is this difference that probably accounts for the differences in fatigue life. (A more complete description of all liner materials is presented in the section Destructive Analysis.) Chamber S/N 60 failed at 34 cycles rather than between 130 and 165 cycles because the test cycle was made much more severe by reducing the coolant flow rate from 0.91 kg/sec to 0.59 kg/sec (2.0 lb/sec to 1.3 lb/sec).

For the extremely severe test cycles, the annealed Amzirc chambers had longer life than did either the OFHC copper or the half-hard Amzirc chambers (Table II). However, when tested at a chamber pressure of 4.4 MN/m^2 (600 psia) and with a coolant flow rate of 0.91 kg/sec (2.0 lb/sec), the OFHC copper chambers had longer life than either of the two Amzirc types.

Structural Analysis

To predict the fatigue life of thrust chambers, the maximum strain range within which the linear material is cycled must be determined. Once this strain range is known, the life of the chamber can be predicted from the material fatigue life curves that are obtained experimentally. These curves present cycles to failure as a function of strain range.

The cyclic strain range to which the liner material is subjected depends upon the mechanical and thermal loading. Mechanical loading is imposed by the coolant channel pressure, the combustion gas pressure, and the thrust load. The thermal loading depends on the thermal gradients that occur in the chamber during its firing cycle. Therefore, to accomplish a structural analysis, a means for predicting the thermal conditions of the structural model must be provided. The thermal analyzer program SINDA[6] was used for the thermal predictions associated with this program. Experimental temperature data were used as an aid in calculating reasonably accurate temperature profiles.

As input, the SINDA program requires hot-gas-side and coolant-side heat transfer boundary conditions as functions of time so that cross-sectional temperature maps may be calculated at selected times during the firing cycle. The heat transfer correlations available in the literature made it possible to describe the boundary conditions accurately for steady-state operation. Two of the nodes in the SINDA program corresponded in location to the measured rib temperature and chamber O.D. temperature locations. The SINDA program, therefore, could be used to extrapolate the experimental data to determine a pseudoexperimental hot-gas-side wall temperature.

When this was done for the design conditions of 4.14-MN/m^2 (600-psia) chamber pressure and 0.91-kg/sec (2.0-lb/sec) coolant flow rate, the hot-gas-side wall temperature was determined to be 828 K (1490° R) instead of the design value of 811 K (1460° R). The difficulty with using an analytical program for a priori temperature prediction, however, is in properly describing the hot-gas-side and coolant-side boundary conditions during the rapid transients. The maximum temperature difference between the hot-gas-side wall and the chamber O.D. occurred during the transients for the cycle used in the present work. Therefore, it was necessary to empirically determine the boundary conditions during the transients in order to force the analytical prediction to match the experimental data. A typical comparison of the analytical temperatures with experimental data is shown in Figure 8. The experimental data, which are represented by the circles, are the rib temperatures measured in the throat plane at a point 1.27 mm (0.050 in.) from the hot-gas-side wall. The triangles represent experimental temperatures measured at the chamber O.D. in the same axial plane. The curves associated with these points are the loci of the analytical temperatures for those locations. Analytical temperature for the hot-gas-side wall is represented by the curve labeled as such, and the temperature difference between the hot-gas-side wall and the chamber O.D. is shown by the ΔT curve. The maximum temperature difference occurs at 0.27 sec into the cycle and the minimum temperature difference occurs at 1.34 sec into the cycle for the case shown.

Table II identifies each chamber, its corresponding test condition, and the nominal rib temperature for each case. Chamber S/N 10 was analyzed separately since its cycle was different from the others. Chambers S/N 40 to S/N 121, which included four OFHC copper chambers, two annealed Amzirc chambers, and two half-hard Amzirc chambers, were all tested under the same conditions. Chambers S/N 60 and S/N 90 were tested at a reduced coolant flow rate and 4.14-MN/m^2 (600-psia) chamber pressure, and chambers S/N 80 and S/N 110 were

tested at 5.52 MN/m^2 (800 psia) and the same reduced coolant flow rate. Each set of test conditions produced a different nominal rib temperature. Therefore, four different thermal analysis cases were required.

Although the thermal analyzer program provides temperatures as a function of time, only two times were selected for the strain analysis. These times corresponded to the points of greatest temperature difference between the hot-gas-side wall and the chamber O.D. during the transient heating and cooling portions of the firing cycle. Generally, this is when the maximum tensile and compressive strains occur. During the heating transient, the thermal growth of the hot copper liner is restricted by the cooler nickel closeout so that large plastic compressive strains are induced in the liner. During the cooling transient, a similar situation occurs except that the closeout is at a higher temperature than the liner and thus tensile strains are induced in the liner. The times of greatest temperature difference are shown in Figure 8 at 0.27 and 1.34 sec.

Figure 3(d) shows the dimensions of a section through the throat of the test chamber. This area was selected for the structural analysis because the high heat flux that occurs here generally produces the maximum strain. Because of symmetry of geometry and loading conditions at the throat plane, the structural analysis could be performed with a model bounded by the inner and outer surfaces and by radial planes through the centers of the channel ribs and coolant channels, as shown in Figure 3(d). This model was used for the finite-element structural program RETSCP[7] that was used in this analysis. Figure 9 is an enlargement of the structural model showing the element identification numbers and their location. The RETSCP program is based on an isoparametric element so that considerably fewer elements are required to model the structure than for programs employing constant-strain triangles.

Table III lists the 34 structural elements and the corresponding theoretical midlife temperatures for the four thermal analysis cases mentioned previously. The progressively increasing temperature with cycles was accounted for in the analysis by selecting a midlife temperature. The heating temperatures are those occurring during the heating transient, and the cooling temperatures are those occurring during the cooling transient.

The boundary conditions for the structural analysis model are shown in Figure 10. As already noted, symmetry boundaries exist along radial planes through the centers of the channel ribs and coolant channels. The displacements of nodes along these planes are taken as zero normal to the planes. All nodes are permitted to move freely in the y or radial direction. The thickness in the axial or z direction is very small so that the thrust chamber axial contour can be neglected. The model is considered to be of constant thickness, and the load in the axial direction is that due to engine thrust. Therefore, a generalized plane strain model is applicable. The surfaces exposed to the coolant and combustion gases have pressure loads normal to those surfaces. This pressure is replaced by force components at each nodal point, as shown in Figure 10. Each node carries load from adjacent pressure surfaces. The force components on the combustion gas surface are zero during the cooling transient because the engine is not being fired.

Materials properties required for the structural analysis were obtained from references 8 and 9. Physical and mechanical properties of the three candidate materials used in this program are documented in these references. Typical properties are presented at room temperature, 27.6 K (50° R), and 810.9 K (1460° R).

The strain range for each element was calculated by first inputting the thermal map for the heating transient into the structural analysis program, along with the appropriate material properties and loading conditions. Total strain and plastic strain were determined for each element. The plastic strains were nonrecoverable (residual strains) and hence became input for the cooling transient analysis. The residual strains were then input with the cooling transient temperature map, and the total and plastic strains were obtained for the combined loading. The strain range was obtained by applying the heating and cooling strains to a theoretical hysteresis loop, as shown in Figure 11.

In Figure 11, the total strain (ε_t^H) in the highly strained elements of the inner wall is in the plastic range during the heating transient. During the cooling transient the state of strain in each element normally reverses along the elastic line until the yield point is reached and then proceeds to a strain of ε_t^c. In the process of this reversal, the strain state passes through a point of zero stress that corresponds to the residual plastic strain (ε_p^H). The strain range is taken as the sum of the total heating and cooling strains less the residual plastic strain.

Table IV lists the strain ranges of each element for the various material and thermal case combinations. The high strain ranges occurred in the hot-gas-side wall region as expected. The maximum strain range occurred at element 30 (see Fig. 9), which is on the hot-gas-side wall centered under the coolant channel. The effective strain range distribution across the model nodes for a typical case is graphically shown in Figure 12.

The maximum strain ranges were used, along with the life curves of Figure 13, to establish the minimum expected life of the chambers. This assumed that the engine failed when a crack appeared in the critical element. However, since all elements below the coolant channel had large strain ranges and a throughcrack had been defined as the criterion for failure, it seemed reasonable to average the strains in this area and to predict life based on this average.

Table V presents the maximum strain range and the average strain range for each case and the corresponding cycles to failure. The actual test cycles to failure are also shown. In every case in which the liner material was annealed Amzirc or half-hard Amzirc, the minimum predicted life and the average predicted life were considerably higher than the actual life of the chamber. This can possibly be explained by the surface pits that were observed on the hot-gas-side wall of the chamber. (A discussion of these observed pits is included in the section Destructive Analysis.) According to reference 11, every small flaw in the material is sur-

rounded by a region where cyclic stresses and strains are larger than the average (nominal) values because of stress concentrations. Consequently, the cyclic plastic strain in these small regions of stress concentration is always larger than the average. The predicted critical strain range does not account for stress concentrations due to cracks or flaws. As a result it could be much smaller than the actual strain range occurring in the vicinity of the flaws. The use of the smaller strain range predicts a life that is longer than would be predicted with the possibly larger actual strain range.

Another possible explanation for the premature failures is the occurrence of cyclic creep, which results from a cyclic mean stress or strain. The most undesirable situation occurs with a cyclically softening material such as half-hard Amzirc. When cyclically softening materials are involved, the damage accumulation is accelerated in two ways. First, the cyclic plastic strain increases from cycle to cycle because of softening. Second, there is a cyclic creep that tends to increase the mean strain toward the maximum available ductility.

From the OFHC copper lives (Table V) it can be seen that in case 1.1 the minimum predicted life is greater than the actual life, in case 2.1 it is less than the actual life, and in case 3.1 it is approximately the same as the actual life. The erratic results lead to the assumption that the material conditions for these chambers were not the same and that the failures may not have been true fatigue failures. It was noted from the structural analysis results that the effective stresses associated with the maximum strain-range element were approximately equal to the ultimate strength of OFHC copper at the elevated temperature occurring during the heating transient. This suggests that it was possible for the coolant pressure to bulge the coolant passage wall to the point of ultimate failure. The physical basis for these assumptions is further discussed in the section Destructive Analysis.

Destructive Analysis

In an attempt to explain the results of the cyclic testing, a destructive analysis was initiated on representative chambers. In addition, some of the test specimens used to acquire the material life curves were analyzed to see if the material conditions were the same as those in the chambers. The results of these investigations follow, along with possible explanations of the discrepancy between the predicted and actual lives.

OFHC Copper Chambers

The failures in the six OFHC copper chambers were not true fatigue failures although they were subjected to a cyclic type of loading. Figure 14 shows that bulging of the channel walls toward the chamber centerline occurred during the cyclic testing. It also shows that there was thinning of the wall and rib in the failure areas. Normally a fatigue failure is associated with crack initiation and consequent crack propagation that may be evidenced by fatigue striations. The bulging and the thinning suggested that the failure mechanism was creep rupture and perhaps thermal ratcheting. Creep rupture is a result of a cyclic mean stress due to unequal loading in tension and compression or unequal tension and compression yield stresses. Thermal ratcheting can be caused by incomplete strain reversal. Once substantial bulging occurs, the thermal and structural characteristics in the vicinity of the bulge change because of the change in geometry. This change in geometry was not accounted for in the thermal and structural analyses, thus introducing a possible source of error. The necking down of a cross section of an OFHC copper chamber failure site is shown in Figure 15. Typical thinning in the failure site was as much as 90%. Other channels in the throat plane thinned from 15 to 20%.

The experimental life of OFHC chamber S/N 10 was 39 cycles, whereas the average life of OFHC chambers S/N 40, 50, 70, and 71 was 150 cycles. Although the firing cycles were not the same, the theoretical maximum strain ranges were almost the same (2.57 and 2.85%). Therefore, theoretically there should have been only a small difference in life. Etched cross sections of the billets from which these chambers were made showed that there was a difference in their grain structure. The billets used to fabricate chambers S/N 40, 50, 70, and 71 had measured ASTM grain sizes varying from approximately 1 to 3. Grain sizes in the billet from which chamber S/N 10 was fabricated were quite large and radially columnar. Measured grain sizes in this billet were much larger than the 0.89-mm (0.035-in.) coolant passage wall thickness. It is obvious that these large columnar grains introduced grain boundaries that extended continuously from the hot-gas-side wall to the coolant passage. These throughgrain boundaries provided weak paths along which premature failures could occur. The chamber S/N 10 billet is shown in Figure 16.

An interesting observation with OFHC copper chamber S/N 40 was evidence of cracking in nonfailure locations in the throat plane. It is possible that these cracks would have propagated to failure if the suspected creep rupture or thermal ratcheting had not already caused failure. Figure 17 shows that these cracks occurred in grain boundaries where it appears that recrystallization has taken place. The indication is that although the failure mode was not fatigue, there was fatigue damage occurring. The strain range in this area (element 34, Fig. 9) and the number of cycles indicated consistent fatigue behavior of the OFHC material.

Amzirc Chambers

Because significant channel wall bulging was not observed in the Amzirc chambers tested, it was presumed that material fatigue was the failure mode. As noted previously, the predicted lives of the Amzirc chambers were much higher than the actual lives. A possible explanation for this discrepancy is that pits were observed in the hot-gas-side walls of the chambers and as a result the material was substantially different from the test specimens for which the life curves were obtained.

Following cyclic testing, surface pits were observed on the hot-gas sides of the Amzirc chamber liners. These visible pits were located randomly over the surface of both the annealed and half-hard Amzirc chambers. Nothing similar was observed with the OFHC copper chambers. Macrophotographs of representative pitted areas of a half-hard Amzirc chamber are shown in Figure 18. The pits were 200 to 400 μm in diameter.

Further investigation of these pitted areas by

electron dispersion analysis showed that the material around the pits had a high zirconium content. It was concluded that the zirconium had not been dispersed uniformly throughout the material and consequently its strengthening potential had not been fully utilized. Furthermore, surface cracking was observed in the pitted areas, as shown in Figures 18(a) and (d), which indicated that the pits were possible locations of stress concentration. Similar investigation of the samples used to obtain the life data in reference 8 showed that the zirconium was uniformly distributed as fine precipitation-strengthening particles rather than as randomly distributed agglomerations of zirconium. This observation confirmed that the test specimen material was not identical to the chamber material with respect to its microstructure. Therefore, the fatigue life curves used to predict the chamber lives were not applicable to these chambers.

A scanning electron micrograph of an Amzirc chamber (chamber S/N 120) fracture surface is shown in Figure 19. The hot-gas-side surface is at the top of the figure. This micrograph clearly shows the existence of fatigue striations in the vicinity of the crack, which confirms the assumption that the Amzirc chambers probably failed in a fatigue failure mode. Also shown at the top center of the micrograph is the crack initiation site. This flaw had a measured length of 1300 μm (0.050 in.) and a depth of 250 μm (0.010 in.), which is approximately one-third of the channel wall thickness. It was speculated that this flaw was present prior to testing and that it was a result of a zirconium-rich grain boundary inclusion. The striations show that the flaw grew in depth with each cycle until it reached the coolant side of the liner wall in approximately 35 cycles. Once it reached this point the crack grew longitudinally until it became large enough to produce a detectable failure.

In contrast to the OFHC copper chambers, there was very little thinning with the Amzirc chambers. With half-hard Amzirc chamber S/N 120 for example, all channels were thinned by only 5 to 10%, including the failure site.

Another difference between the reference Amzirc test specimen material and the chamber material was found for the half-hard material cases. The half-hard Amzirc test specimens of reference 8 has an as-fabricated hardness of Rockwell B (R_B) 45 to 46; but the chambers had an as-fabricated hardness of R_B 68 to 70, indicating much more cold working of the chamber material during fabrication.

The test specimen results of reference 8 signified that cold working the Amzirc improved the fatigue life of the material. This was true even though the specimens eventually strain softened to R_B 0 at their fracture sites. The half-hard Amzirc chambers of this project did not demonstrate any advantage of cold working on fatigue life. They started out harder than the specimens of reference 8 (R_B 68 to 70 versus R_B 45 to 46) and were harder at their fracture sites (R_B 56 and R_B 10 versus R_B 0). The half-hard Amzirc chambers were cycled to two different nominal temperatures. After 82 cycles up to 828 K (1490° R), chamber S/N 120 strain softened to R_B 56 at the fracture site. After 21 cycles up to 1194 K (2150° R), chamber S/N 110 softened to R_B 10 at the fracture site. With both chambers the hardness remained as fabricated in cooler regions away from the fracture site. The conclusion is that strain softening did occur in half-hard Amzirc chambers near the hot-gas-side wall. The amount of strain softening appears to be related to the hot-gas-side wall temperature. The advantage of hardening the Amzirc chamber material by cold working during fabrication was not realized, although it had been expected from the data of reference 8. The reason may be related to differences in the material discussed earlier.

Concluding Remarks

Present capabilities in predicting the low-cycle thermal fatigue life of rocket combustion chambers are limited by the following factors:

1. The inability to predict wall temperatures during the start and shutdown transients of the test cycle
2. The inability to fabricate a chamber so that the microstructure of the material is identical to that of the laboratory test specimen used to determine the fatigue life characteristics of the material

For the first factor, it is obvious that valid life predictions can be obtained only if proper structural analysis yields accurate strain-range predictions. For test cycles where the temperature difference between the hot-gas-side wall and the chamber O.D. maximizes during a rapid start transient, the strain range will also maximize during this transient. If an a priori analysis is required, then a rigorous heat transfer analysis must be made for the transients, since this is the life-limiting condition.

Presently the heat transfer analysis during the transient is hampered by insufficient knowledge as to how the coolant coefficient and the hot-gas-side coefficient vary during startup and shutdown.

For the second limiting factor, better material processing and material property control are needed. In selecting chamber materials, the zirconium-copper alloys must continue to be considered. Improved fatigue life for these alloys has been demonstrated in reference 8. The material processing and material property control in this present work were inadequate and the potential for the alloys was not realized. In fact, the fatigue life demonstrated was no better than if the material had not been alloyed at all. The fatigue life of most of the zirconium-copper alloy chambers would have been accurately predicted if the OFHC copper life curves had been used. The implication is that the alloying of the isothermal test specimens was done properly because there was a significant improvement in fatigue life over OFHC copper. But with the combustion chambers, the alloying was not effective and the potential advantage over OFHC was not realized. The fatigue life potential of copper alloys makes them the best choice for use as high-pressure, long-life rocket combustion chambers, but better material processing control is needed.

Summary of Results

During a test program to investigate low-cycle thermal fatigue, 13 rocket combustion chambers were fabricated and cyclically test fired to failure. Chamber liners were fabricated of copper or copper alloy and had milled coolant channels. The chambers were completed by means of an electroformed

nickel closeout. The combustion chamber pressures were 4.16 and 5.52 MN/m^2 (600 and 800 psia). The oxidant-fuel ratio for the liquid oxygen and gaseous hydrogen propellants was 6.0. The following results were obtained:

1. The failures in the oxygen-free, high-conductivity (OFHC) copper chambers were not typical fatigue failures but are best described as ratcheting-enhanced creep rupture. The coolant channels bulged toward the chamber centerline and progressive thinning of the wall was produced during each cycle as a result.

2. The Amzirc chambers failed by low-cycle thermal fatigue.

3. The unexpected short life of the Amzirc chambers as compared with the predicted life was attributed to an unexpected difference in the chamber material from the material tested by Mar-Test, Inc. Although zirconium was present in the same concentration, its distribution was not uniform.

4. Crack propagation was rather rapid in two of the annealed Amzirc chambers once a throughcrack was present, growing at an average rate of 1.2 mm/cycle (0.045 in./cycle).

5. Some strain softening did occur in the half-hard Amzirc chambers near the hot-gas-side wall. The amount of strain softening appeared to be related to the hot-gas-side wall temperature.

6. An OFHC liner fabricated from a billet with large radially columnar grains had a life of only 39 cycles, whereas under identical test conditions OFHC liners fabricated from fine-grained billets had average lives of 150 cycles.

7. With OFHC copper combustion chamber liners, some recrystallization of grains at the hot-gas-side surface occurred and was accompanied by surface cracking.

8. There was a trend of increasing measured rib temperature, chamber O.D. temperature, and coolant temperature rise from the first cycles to the last cycles of chamber life. The amount of this increase seemed to be related to the amount of deformation, which in turn was related to the strength of the liner material used.

9. With the OFHC copper liners, two different chamber contours were cyclically tested and there was no effect observed on life.

10. Between cycles a leak as small as 1 wall thickness in diameter produced a distinct sound that was detectable and was recorded on an audio tape. From a review of the audio tape the exact cycle during which a failure occurred could be determined.

References

1. Goalwin, D. S., "A High-Pressure Regeneratively Cooled Thrust Chamber. Volume 1: Analysis, Test, and Evaluation," R-7646-1, Aug. 1969, Rocketdyne, Canoga Park, Calif. (AFRPL-TR-68-226-Vol-1; AD-504321L).

2. Kaufmann, M., "A High-Pressure, Regeneratively Cooled Thrust Chamber. Volume 2: Design and Manufacturing Report," MBB-TR-900, Aug. 1968, Messerschmitt-Boelkow-Blohm GmbH, Munich (West Germany) (AFRPL-TR-68-226-Vol-2; AD-507172L).

3. Fulton, D., "Investigation of Thermal Fatigue in Non-Tubular Regeneratively Cooled Thrust Chambers, Volume 1," R-9093-Vol-1, May 1973, Rockwell International Corp., Canoga Park, Calif. (AD-760582; AFRPL-TR-73-10-Vol-1).

4. Fulton, D., "Investigation of Thermal Fatigue in Non-Tubular Regeneratively Cooled Thrust Chambers, Volume 2," R-9093-Vol-2, May 1973, Rockwell International Corp., Canoga Park, Calif. (AD-760583; AFRPL-TR-73-10-Vol-2).

5. Andrews, J. S. and Armstrong, W. H., "3.3 K Thrust Chamber Life Prediction," D180-18170-1, Aug. 1974, Boeing Aerospace Co., Seattle, Wash.

6. Smith, J. P., "SINDA User's Manual," TRW-14690-H001-R0-00, Apr. 1971, TRW Systems Group (NAS9-10435), Redondo Beach, Calif.

7. Miller, R. W., "RETSCP: A Computer Program for Analysis of Rocket Thermal Strains with Cyclic Plasticity," June 1974, Atkins and Merrill, Inc., Ashland, Mass; also CR-134640, May 1974, NASA.

8. Conway, J. B., Stentz, R. H. and Berling, J. T., "High Temperature, Low Cycle Fatigue of Copper-Base Alloys in Argon. Part I: Preliminary Results for 12 Alloys at 1000° F (538° C)," Jan. 1973, Mar-Test Inc., Cincinnatti, Oh.; also CR-121259, Aug. 1973, NASA.

9. Esposito, J. J. and Zabora, R. F., "Thrust Chamber Life Prediction: Volume I: Mechanical and Physical Properties of High Performance Rocket Nozzle Materials," D180-18673-Vol-1, Boeing Aerospace Co., Seattle, Wash.; also CR-134806, Apr. 1975, NASA.

10. Pritz, W., George, D., and Evans, S. A., "The JANNAF Rocket Engine Performance Prediction and Evaluation Manual," CPIA-Publ-246, Apr. 1975, Chemical Propulsion Information Agency, Johns Hopkins Univ., Baltimore, Md.

11. Sandor, B. I., Fundamentals of Cyclic Stress and Strain, The University of Wisconsin Press, Wisc., 1972.

TABLE I. - TEST MATRIX

Chamber pressure, MN/m^2 (psia)		4.14(600)	4.14(600)	4.14(600)	5.52(800)
Coolant flow rate, kg/sec (lb/sec)		0.91(2.0)	0.91(2.0)	0.59(1.3)	0.59(1.3)
Cycle		Slow	Fast	Fast	Fast
OFHC liner material	Contour A	------	S/N 70	S/N 60	-------
		------	S/N 71	------	-------
	Contour B	S/N 10	S/N 40	------	-------
		------	S/N 50	------	-------
Annealed Amzirc liner material	Contour A	------	S/N 100	S/N 90	S/N 80
		------	S/N 101	------	-------
Half-hard Amzirc liner material	Contour A	------	S/N 120	------	S/N 110
		------	S/N 121	------	-------

TABLE II. - NOMINAL TEST CONDITIONS AND EXPERIMENTAL DATA

Chamber S/N	Liner material	Experimental data					Nominal test conditions[a]						Thermal analysis case	Strain analysis case	Remarks
		Hottest rib temperature				Number of cycles to failure	Coolant flow rate		Chamber pressure		Rib temperature				
		New		End											
		K	°R	K	°R		kg/sec	lb/sec	MN/m²	psia	K	°R			
[b]10	OFHC copper	606	1090	----	1250	39	0.91	2.0	4.14	600	656	1180	1	1.1	Additional 13 cycles put on after first failure (130 cycles); three additional pin holes discovered after retest
40	↓	---	----	----	----	165	↓	↓	↓	↓	639	1150	2	2.1	↓
50		---	----	626	1127	130					↓	↓	↓	↓	
70		611	1100	639	1150	152									
71		---	----	----	----	151									
100	Annealed Amzirc	---	----	----	----	[c]63								2.2	Three failures discovered at same time
101	Annealed Amzirc	644	1160	686	1235	---								2.2	Premature failure - two plugged channels
120	Half-hard Amzirc	---	----	----	----	82								2.3	
121	Half-hard Amzirc	611	1100	611	1100	65								2.3	
60	OFHC copper	---	----	1420	1643	34	0.59	1.3	4.14	600	833	1500	3	3.1	
90	Annealed Amzirc	789	1420	1420	1443	[c]85			4.14	600	833	1500	3	3.2	Four failures discovered at same time
80	Annealed Amzirc	---	----	----	----	77			5.52	800	947	1705	4	4.1	
110	Half-hard Amzirc	928	1670	967	1740	21	↓	↓	5.52	800	947	1705	4	4.2	Surface melted at crack site

[a]Coolant inlet temperature, 33 K(60° R) for all tests.
[b]Slow cycle; all others are fast cycle.
[c]Some uncertainty as to when first failure occurred.

TABLE III. - ELEMENT TEMPERATURES FOR HEATING AND COOLING TRANSIENTS

Element	Case 1				Case 2				Case 3				Case 4			
	Heat		Cool		Heat		Cool		Heat		Cool		Heat		Cool	
	K	°R	K	°R	K	°R	K	°R	K	°R	K	°R	K	°R	K	°R
1	193	347	203	365	82	147	253	455	89	161	323	581	96	172	351	632
2	193	347	203	365	82	147	253	455	90	162	323	581	96	172	351	632
3	193	347	203	365	82	147	253	455	90	162	323	581	96	172	351	632
4	261	470	156	281	191	342	189	340	171	308	248	447	239	428	262	472
5	288	518	153	276	219	395	186	335	254	457	244	439	281	505	258	464
6	298	537	153	276	230	414	185	334	268	481	243	438	297	534	257	462
7	408	735	131	236	390	703	144	260	472	850	197	354	537	967	203	365
8	416	749	130	234	395	712	146	262	478	861	198	357	545	981	204	368
9	453	816	123	222	452	814	137	245	549	989	188	339	628	1131	193	347
10	459	827	125	225	455	819	138	249	553	996	189	341	633	1139	194	350
11	546	983	117	210	560	1007	130	234	687	1237	180	324	794	1430	183	330
12	552	993	118	212	562	1011	131	236	690	1242	181	326	799	1438	185	333
13	612	1101	114	205	629	1133	128	230	777	1398	178	320	906	1630	181	325
14	614	1106	115	207	628	1130	129	232	776	1396	179	322	904	1628	182	327
15	738	1330	109	197	766	1378	124	224	956	1720	173	312	1128	2031	176	316
16	730	1314	110	198	755	1358	124	224	942	1695	174	313	1111	2000	177	318
17	708	1276	111	200	730	1314	126	226	909	1637	175	315	1071	1928	178	320
18	681	1227	113	203	698	1256	127	229	867	1561	177	318	1019	1834	179	323
19	671	1208	114	205	685	1233	128	230	850	1531	178	320	999	1798	181	325
20	748	1347	110	198	773	1391	125	225	965	1737	174	313	1142	2054	176	317
21	744	1339	110	198	768	1382	125	225	959	1726	174	313	1133	2040	177	318
22	722	1299	111	200	750	1351	126	226	936	1685	175	315	1106	1990	177	319
23	696	1253	113	203	710	1279	127	229	884	1592	177	319	1041	1874	180	324
24	690	1243	113	204	756	1361	127	228	876	1577	178	320	1117	2010	179	322
25	770	1385	110	198	790	1422	126	226	988	1779	174	314	1171	2108	177	319
26	766	1378	110	198	786	1414	126	226	983	1769	175	315	1164	2096	177	318
27	748	1346	111	200	764	1376	127	228	955	1719	176	316	1131	2035	178	321
28	732	1317	112	202	745	1341	127	229	930	1674	177	318	1099	1979	179	323
29	727	1309	112	202	740	1333	127	229	924	1663	177	319	1092	1965	180	324
30	795	1431	109	196	814	1464	126	226	1019	1835	174	314	1212	2181	177	319
31	784	1412	110	198	801	1442	126	227	1003	1806	176	316	1192	2146	178	320
32	770	1396	111	199	790	1422	127	228	989	1781	176	316	1175	2115	178	321
33	764	1376	111	200	777	1399	127	229	973	1751	177	318	1154	2078	179	322
34	758	1364	111	200	770	1386	127	229	963	1733	177	318	1143	2057	179	323

TABLE IV. - ELEMENT STRAIN RANGES FOR VARIOUS MATERIAL AND THERMAL CASE COMBINATIONS

Element	Strain range, percent							
	Case							
	1.1	2.1	2.2	2.3	3.1	3.2	4.1	4.2
1	0.19	0.34	0.26	0.26	0.32	0.31	0.36	0.36
2	.19	.34	.25	.27	.33	.33	.36	.36
3	.20	.36	.26	.28	.34	.34	.38	.39
4	.22	.28	.28	.27	.23	.24	.24	.23
5	.24	.24	.24	.23	.17	.18	.19	.26
6	.25	.23	.23	.21	.17	.17	.18	.26
7	.51	.41	.42	.41	.47	.48	.58	.57
8	.52	.42	.42	.43	.49	.49	.60	.58
9	.63	.57	.57	.56	.66	.69	.84	.79
10	.67	.60	.62	.57	.71	.76	.91	.84
11	.78	.72	.74	.71	.87	.88	1.07	1.04
12	.79	.73	.75	.73	.87	.89	1.08	1.05
13	.93	.89	.92	.90	1.10	1.12	1.35	1.37
14	.86	.82	.82	.81	.99	.98	1.21	1.21
15	2.25	2.58	2.55	2.58	3.24	3.20	3.84	3.88
16	2.42	2.79	2.78	2.42	3.47	3.46	4.12	3.94
17	2.26	2.59	2.64	1.72	3.23	3.27	3.93	3.65
18	1.54	1.66	1.69	1.30	2.10	2.15	2.68	2.68
19	1.22	1.21	1.24	2.48	1.55	1.60	1.96	2.00
20	2.37	2.70	2.69	2.39	3.36	3.34	3.98	3.80
21	2.26	2.57	2.60	2.09	3.21	3.22	3.86	3.65
22	1.91	2.13	2.15	2.09	2.71	2.72	3.28	3.21
23	1.77	2.03	2.05	2.09	2.52	2.55	3.20	3.24
24	1.59	1.83	1.86	1.96	2.17	2.22	2.94	3.03
25	2.45	2.76	2.79	2.49	3.42	3.44	4.12	3.82
26	2.24	2.49	2.51	2.34	3.12	3.15	3.80	3.61
27	2.03	2.22	2.25	2.23	2.82	2.84	3.48	3.45
28	1.89	2.11	2.11	2.18	2.68	2.67	3.30	3.41
29	1.83	2.00	1.99	2.12	2.59	2.58	3.11	3.26
30	2.57	2.85	2.91	2.58	3.54	3.60	4.34	3.97
31	2.27	2.49	2.55	2.36	3.14	3.18	3.89	3.67
32	2.07	2.28	2.28	2.30	2.89	2.90	3.58	3.62
33	2.07	2.27	2.25	2.35	2.94	2.92	3.57	3.74
34	2.05	2.23	2.20	2.34	2.91	2.86	3.46	3.63

TABLE V. - THEORETICAL STRAIN RANGES AND LIFE PREDICTIONS COMPARED WITH EXPERIMENTAL LIVES

Case	Liner material	Strain range, percent		Predicted cycles to failure		Actual (experimental) cycles to failure
		Maximum	Average	[a]Minimum	Average	
1.1	OFHC copper	2.57	2.26	76	100	39
2.1	OFHC copper	2.85	2.54	60	78	[b]150
2.2	Annealed Amzirc	2.91	2.56	330	480	63
2.3	Half-hard Amzirc	2.58	2.39	840	1000	[c] 74
3.1	OFHC copper	3.54	3.18	37	47	34
3.2	Annealed Amzirc	3.60	3.19	193	260	85
4.1	Annealed Amzirc	4.34	3.85	125	163	77
4.2	Half-hard Amzirc	3.97	3.69	335	390	21

[a]Based on maximum strain.
[b]Average of four specimens.
[c]Average of two specimens.

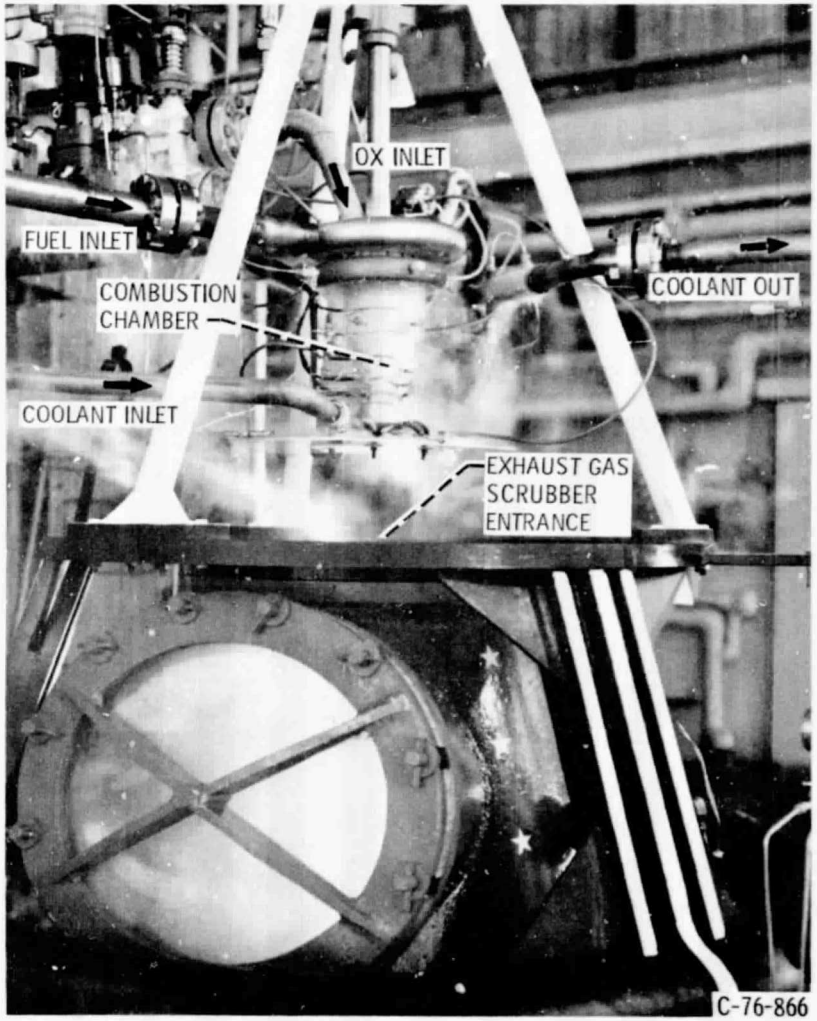

(a) PHOTOGRAPH OF TEST COMBUSTION CHAMBER AND THRUST STAND.

Figure 1. - Test facility.

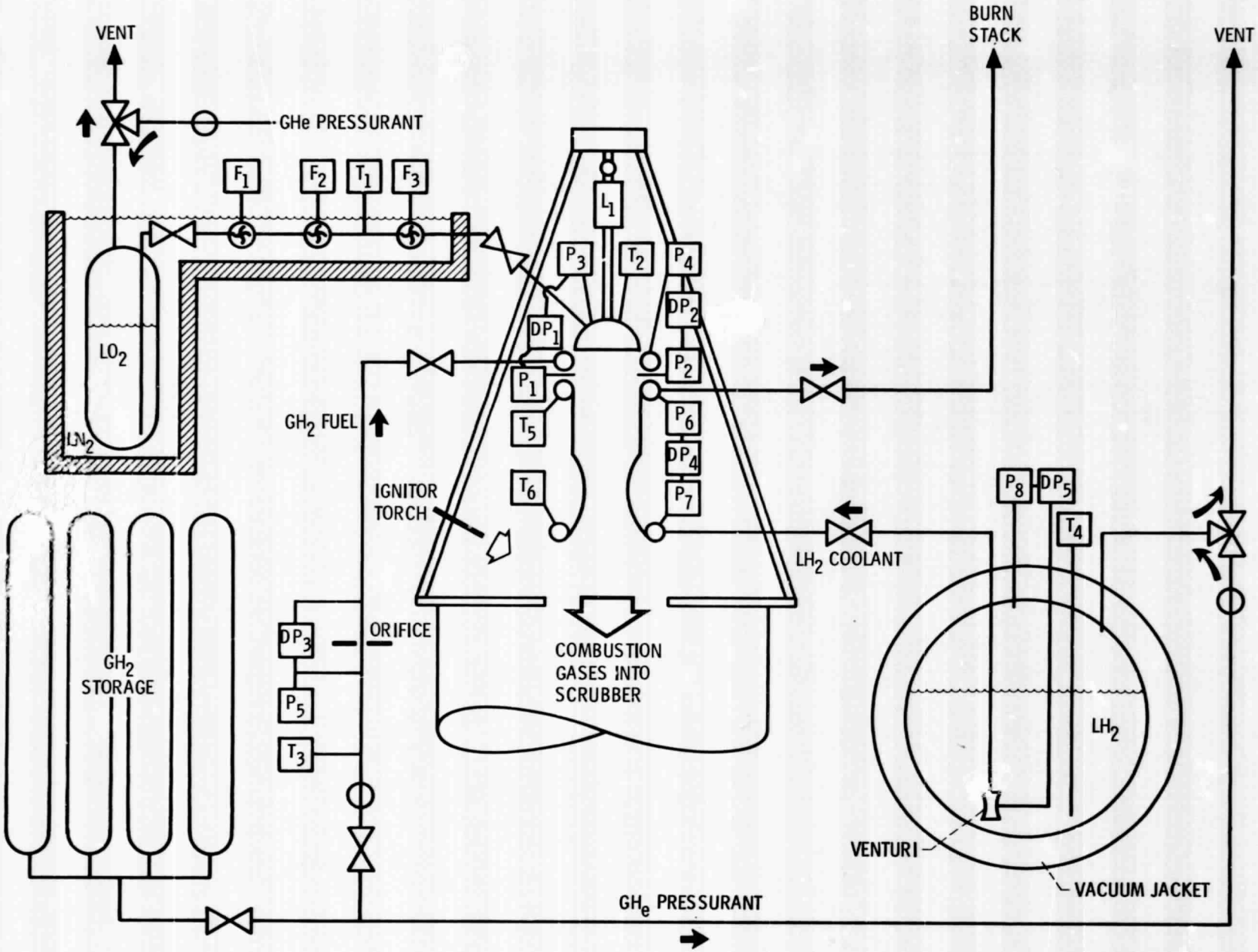

(b) SCHEMATIC OF TEST FACILITY.

Figure 1. - Continued.

L_1	THRUST, STRAIN-GAUGE-BRIDGE TYPE LOAD-CELL
F_1, F_2, F_3	OXIDIZER FLOW, TURBINE TYPE FLOW METERS
P_1, P_2	COMBUSTION CHAMBER PRESSURE, STRAIN-GAUGE-BRIDGE TYPE PRESSURE TRANSDUCER
P_3	OXIDIZER INJECTION PRESSURE, "
P_4	FUEL INJECTION PRESSURE, "
P_5	FUEL ORIFICE PRESSURE, "
P_6	COOLANT OUTLET PRESSURE, "
P_7	COOLANT INLET PRESSURE, "
P_8	COOLANT TANK PRESSURE, "
T_1	OXIDIZER TEMPERATURE AT FLOWMETERS, PLATINUM RESISTANCE BRIDGE TRANSDUCER
T_2	OXIDIZER INJECTION TEMPERATURE, PLATINUM RESISTANCE BRIDGE TRANSDUCER
T_3	FUEL TEMPERATURE AT ORIFICE, COPPER/CONSTANTAN THERMOCOUPLE
T_4	COOLANT TEMPERATURE AT VENTURI, PLATINUM RESISTANCE BRIDGE TRANSDUCER
T_5	COOLANT OUTLET TEMPERATURE, CHROMEL/CONSTANTAN THERMOCOUPLE
T_6	COOLANT INLET TEMPERATURE, PLATINUM RESISTANCE BRIDGE TRANSDUCER
DP_1	OXIDIZER INJECTOR PRESSURE DROP, STRAIN-GAUGE-BRIDGE TYPE PRESSURE TRANSDUCER
DP_2	FUEL INJECTOR PRESSURE DROP, "
DP_3	FUEL ORIFICE PRESSURE DROP, "
DP_4	COOLANT JACKET PRESSURE DROP, "
DP_5	COOLANT VENTURI PRESSURE DROP, "

(c)

Figure 1. - Concluded.

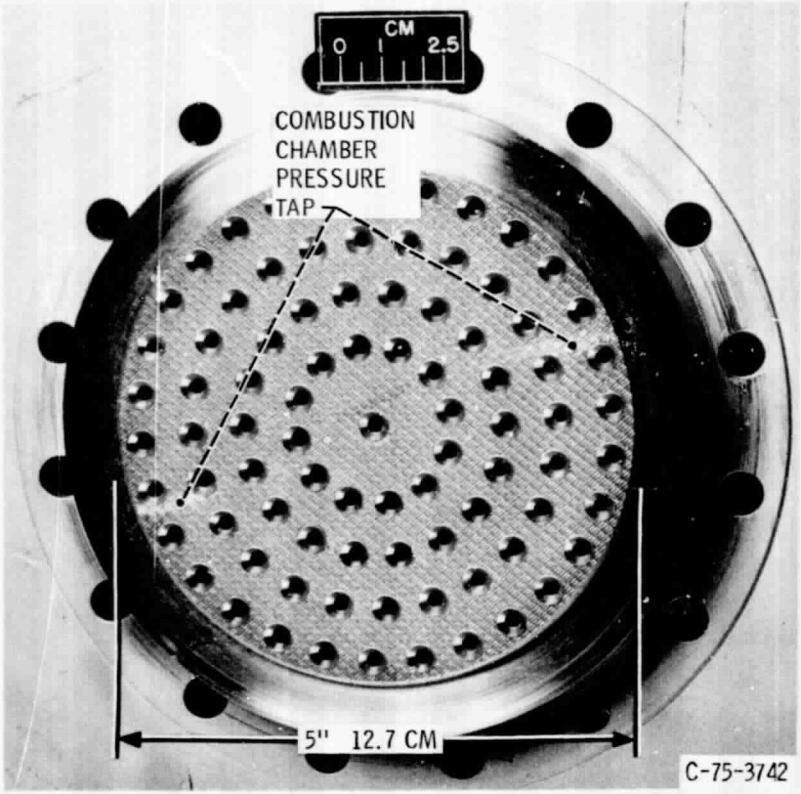

(a) PHOTOGRAPH OF INJECTOR FACE.
Figure 2. - Injector.

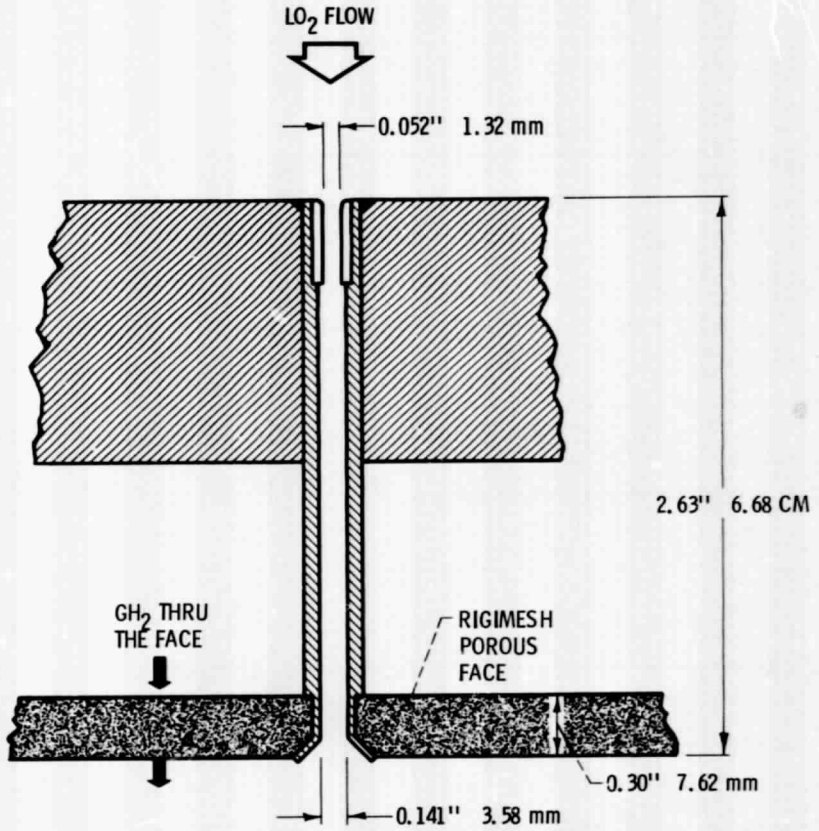

(b) SKETCH OF INJECTOR ELEMENT.
Figure 2. - Concluded.

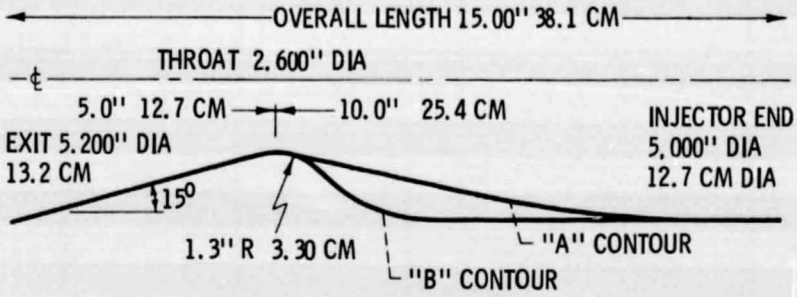

(a) COMPARISON OF CONTOURS.

Figure 3. - Fatigue chambers.

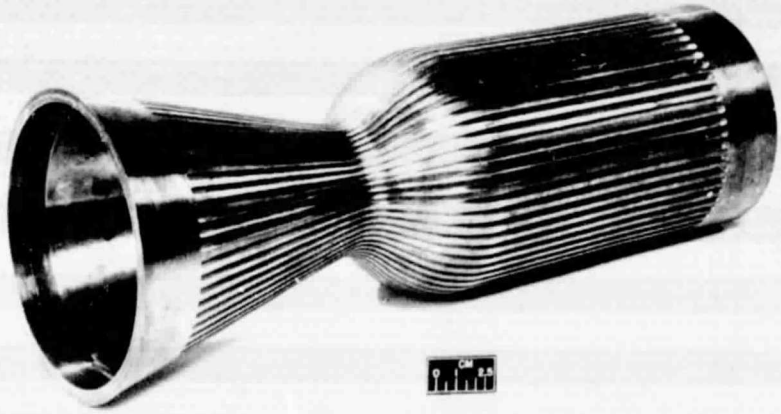

(b) PHOTOGRAPH OF CHAMBER LINER (CONTOUR "B").

Figure 3. - Continued.

(c) PHOTOGRAPH OF CLOSED OUT LINER (CONTOUR "B").

Figure 3. - Continued.

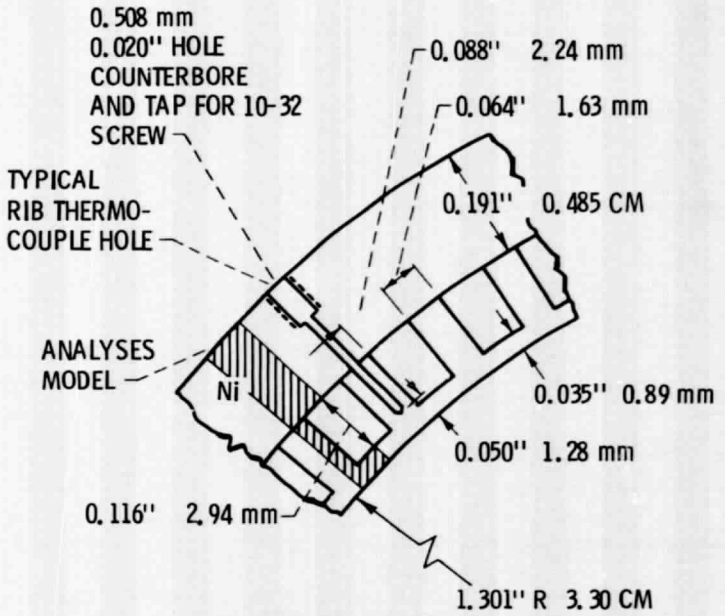

(d) THROAT CROSS SECTION.

Figure 3. - Continued.

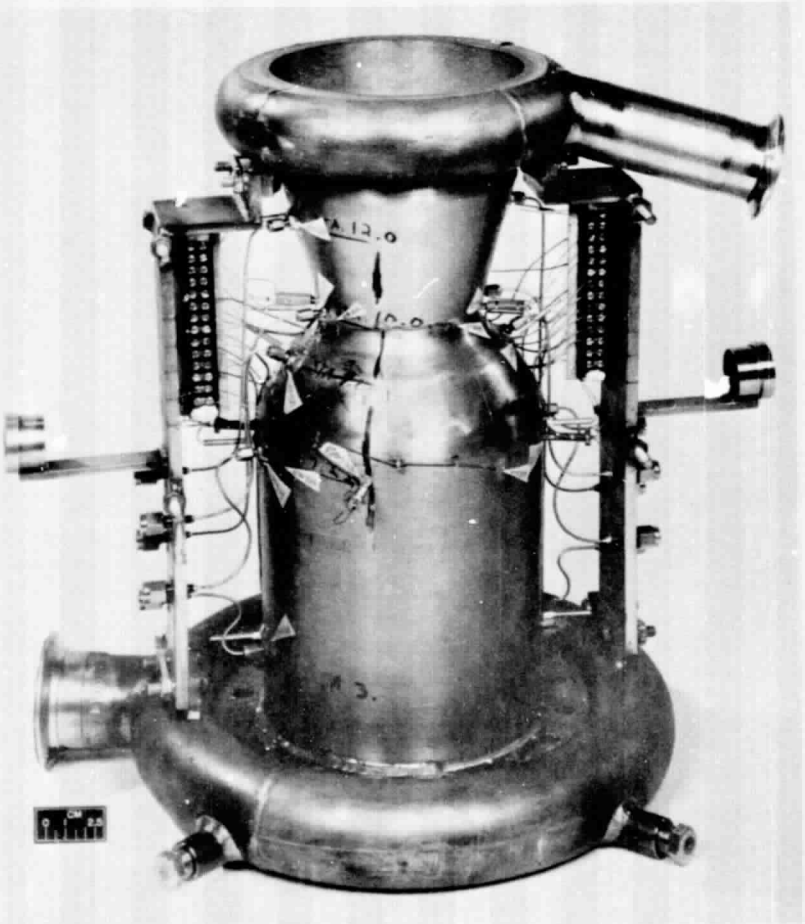

(e) COMPLETED FATIGUE CHAMBER (CONTOUR B).

Figure 3. - Continued.

C-76-1026

(f) COMPLETED FATIGUE CHAMBER (CONTOUR A).

Figure 3. - Concluded.

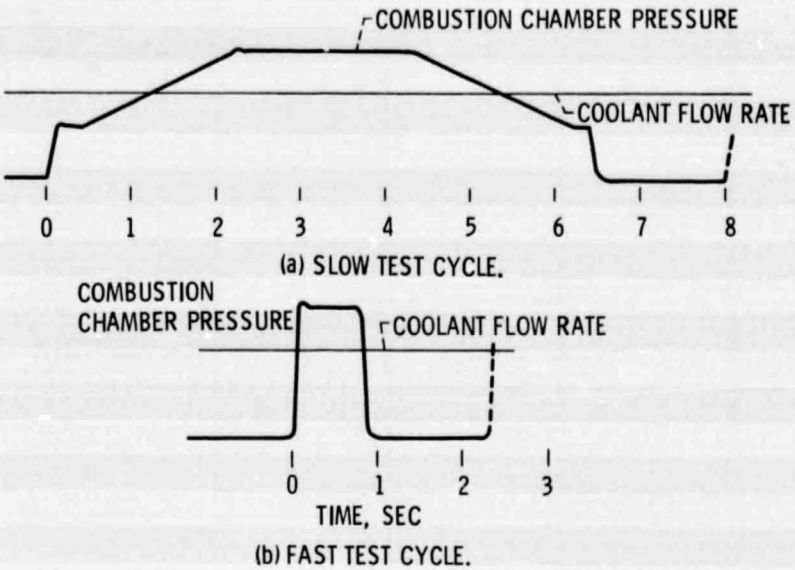

Figure 4. - Schematic comparison of two different duty cycles used in fatigue testing of rocket chambers.

E-8745

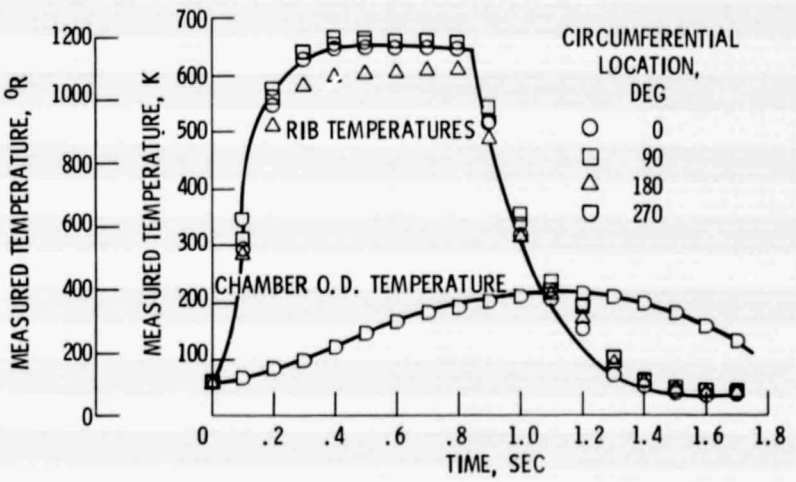

Figure 5. - Measured rib temperatures and chamber O.D. temperature as function of time for one firing cycle. Chamber S/N 70.

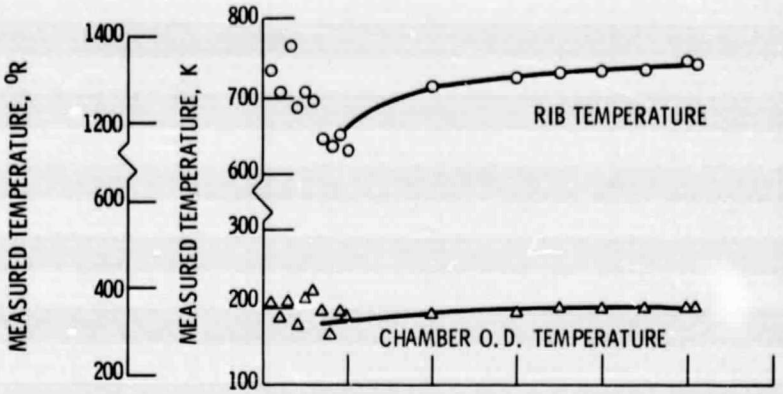

(a) SUMMARY OF RIB AND CHAMBER O.D. TEMPERATURES FOR EACH LIFE CYCLE.

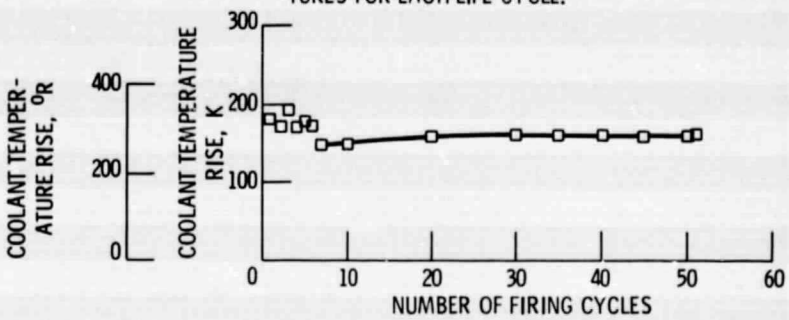

(b) SUMMARY OF COOLANT TEMPERATURE RISE DATA FOR EACH LIFE CYCLE.

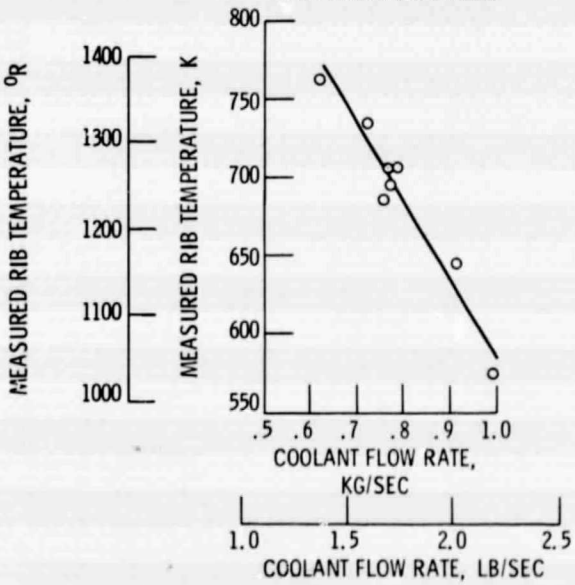

(c) EFFECT OF COOLANT FLOW RATE ON MEASURED RIB TEMPERATURE.

Figure 6. - Experimental data, Chamber S/N 101.

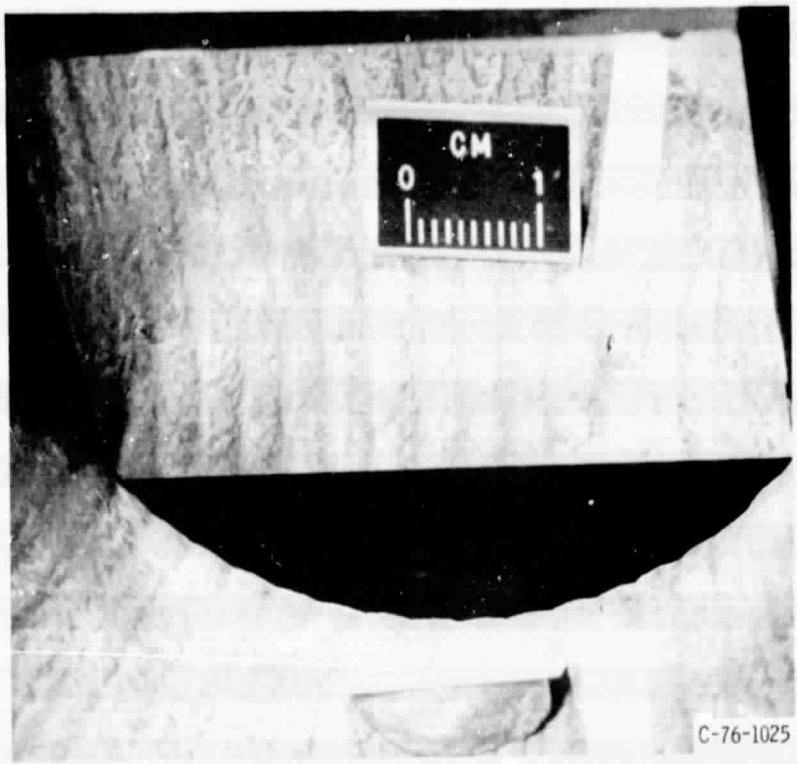

(a) CHAMBER S/N 50 - OFHC COPPER.

Figure 7. - Typical fatigue failure sites.

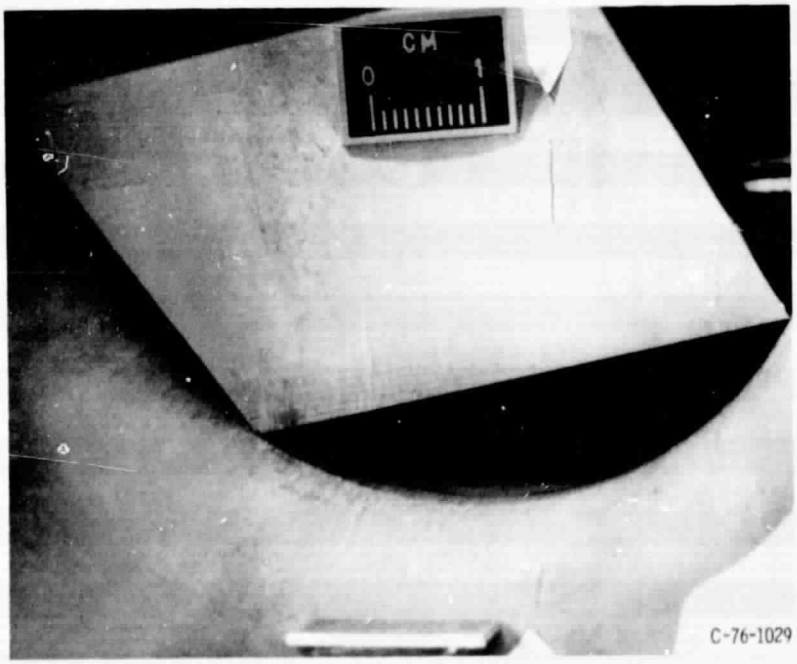

(b) CHAMBER S/N 121 - 1/2 HARD AMZIRC.

Figure 7. - Continued.

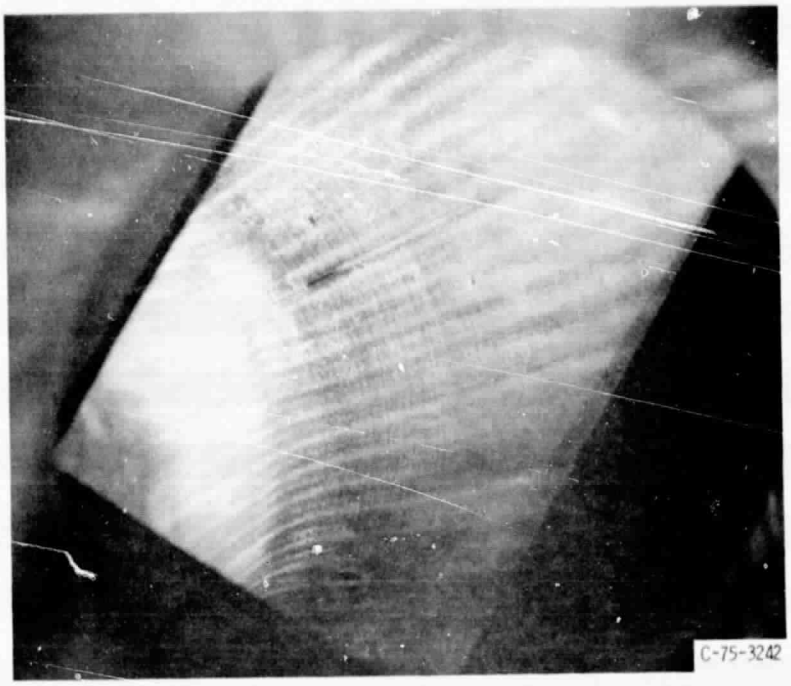

(c) CHAMBER S/N 80 - AMZIRC - 2 CYCLES AFTER FAILURE.

Figure 7. - Continued.

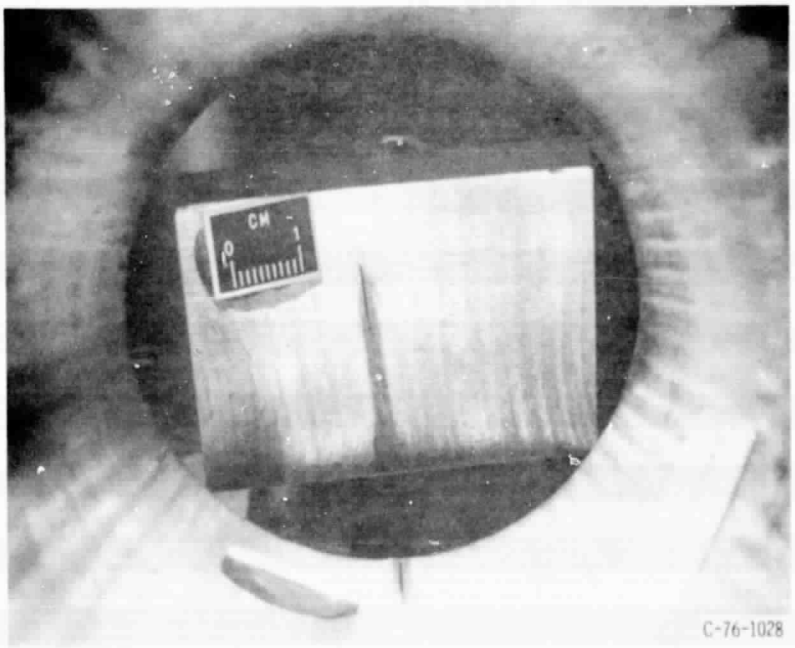

(d) CHAMBER S/N 80 - AMZIRC - 12 CYCLES AFTER FAILURE.

Figure 7. - Continued.

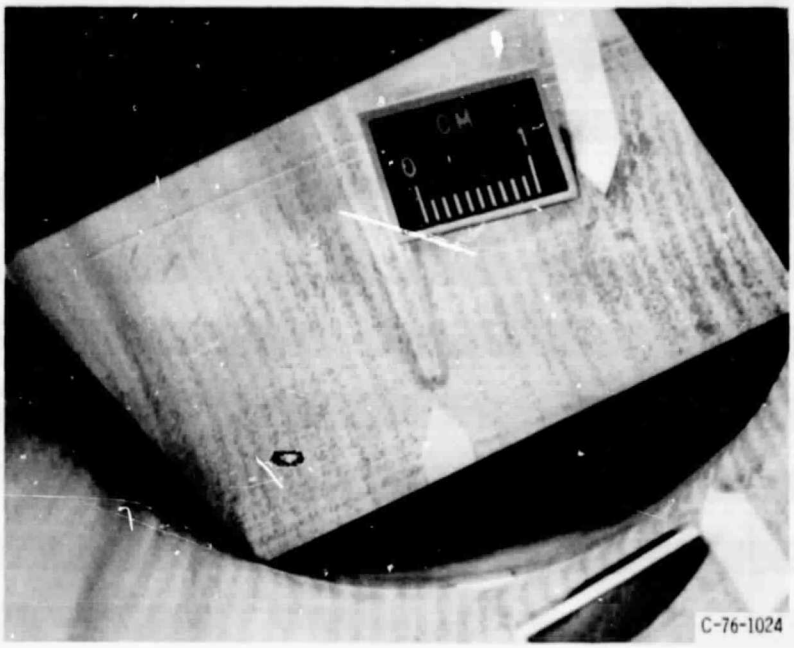

(e) CHAMBER S/N 100 - AMZIRC.

Figure 7. - Concluded.

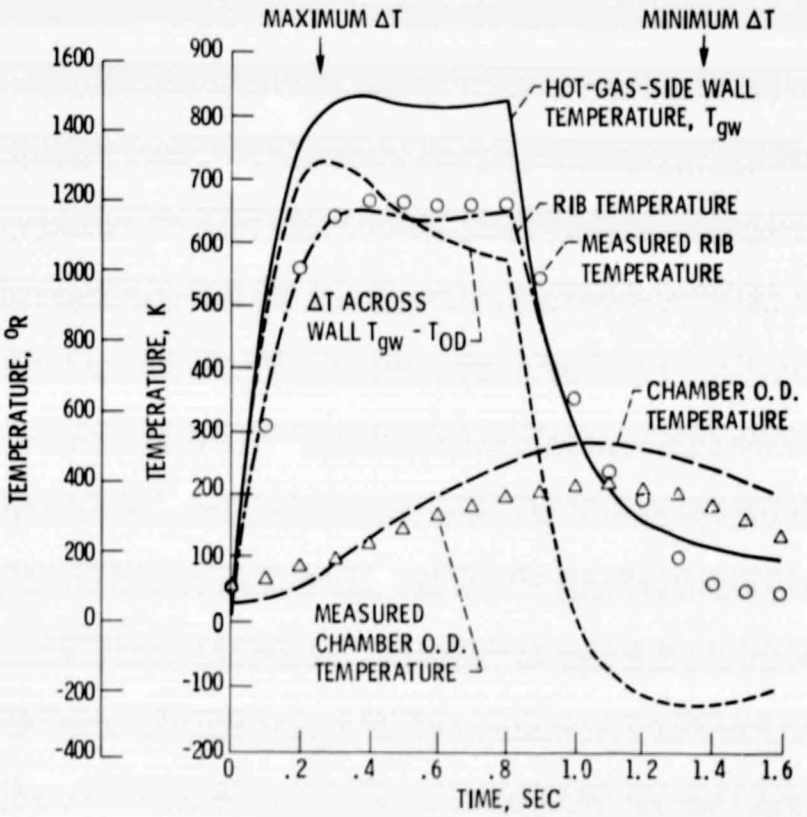

Figure 8. - Typical matching of thermal analysis to experimental data.

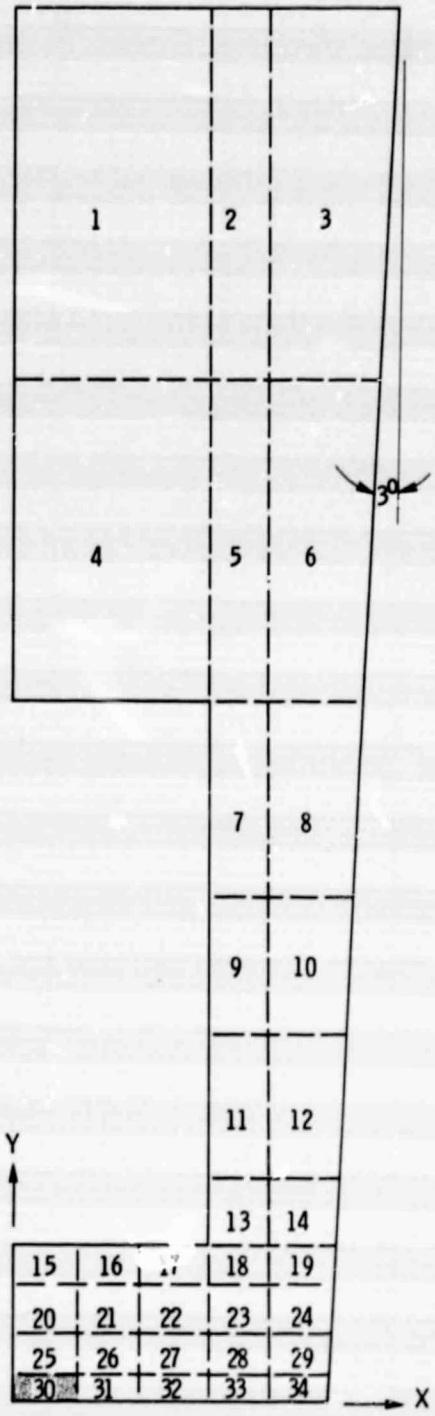

Figure 9. - Structural model with element numbers.

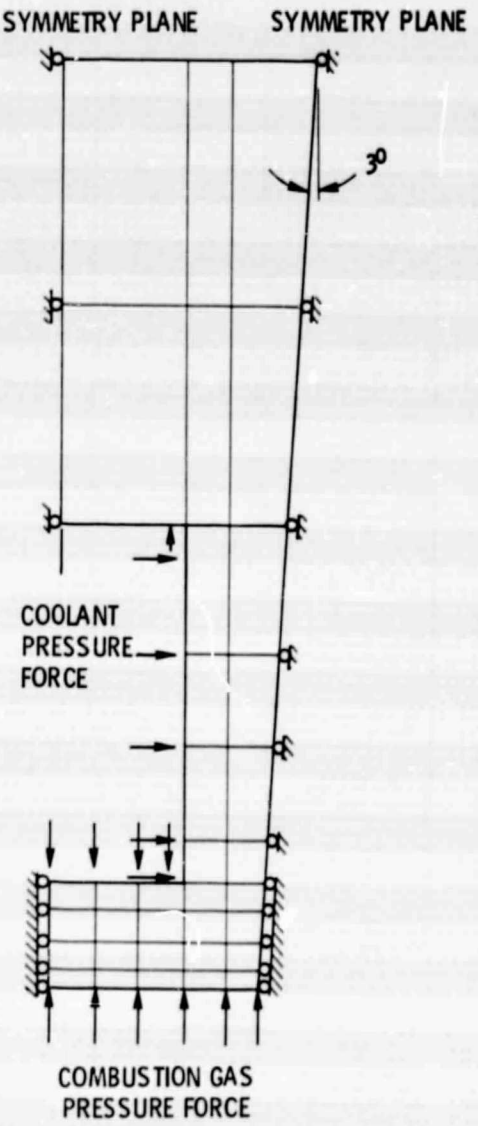

Figure 10. - Force and displacement (symmetry) boundary conditions.

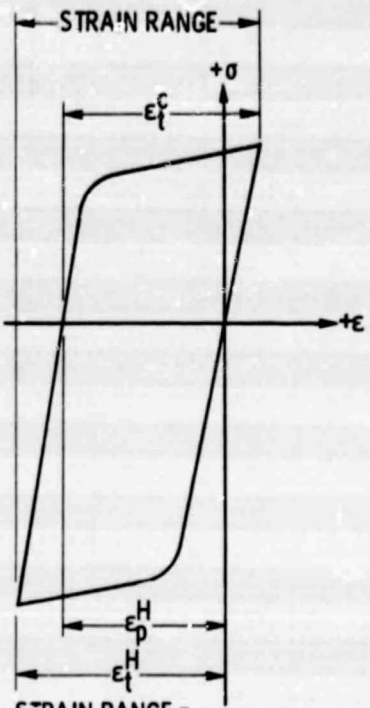

STRAIN RANGE =
$\varepsilon_t^H + (\varepsilon_t^c - \varepsilon_p^H)$

WHERE:

ε_t^H = TOTAL STRAIN DURING HEATING

ε_p^H = PLASTIC STRAIN DURING HEATING

ε_t^c = TOTAL STRAIN DURING COOLING

Figure 11. - Theoretical stress-strain hysteresis loop.

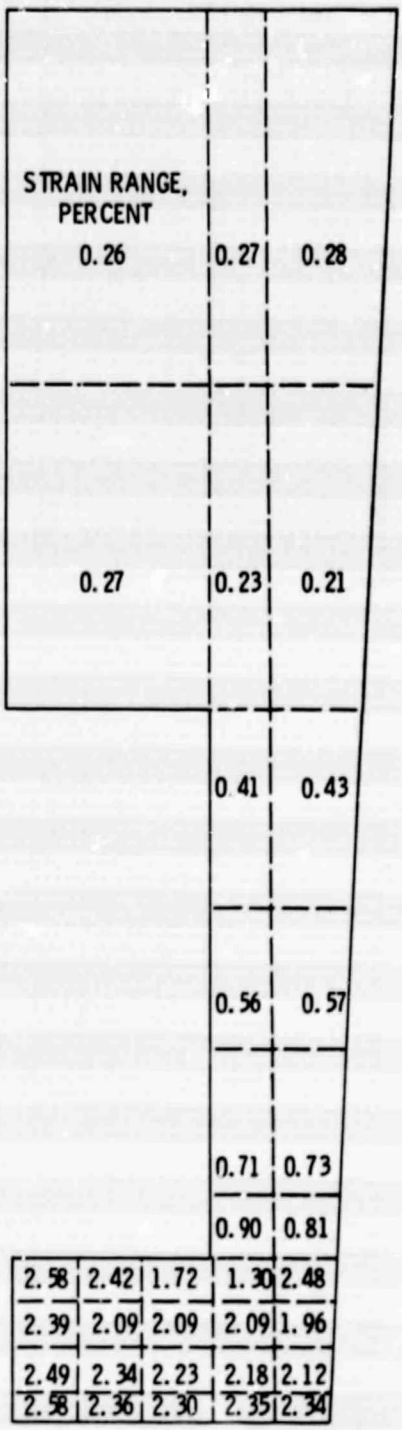

Figure 12. - Effective strain range distribution for case 2.3.

E-8745

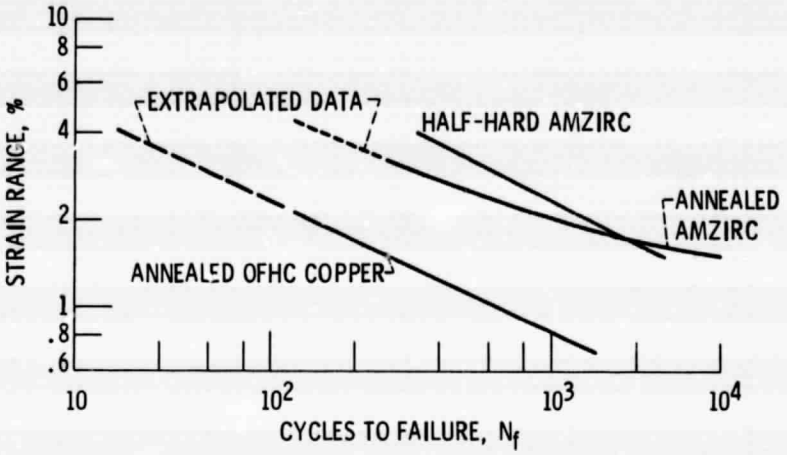

Figure 13. - Typical low-cycle fatigue life of annealed OFHC copper, annealed Amzirc, and half-hard Amzirc. $\dot{\varepsilon} = 0.002\ sec^{-1}$; 538 K ($1460^{o}$ R).

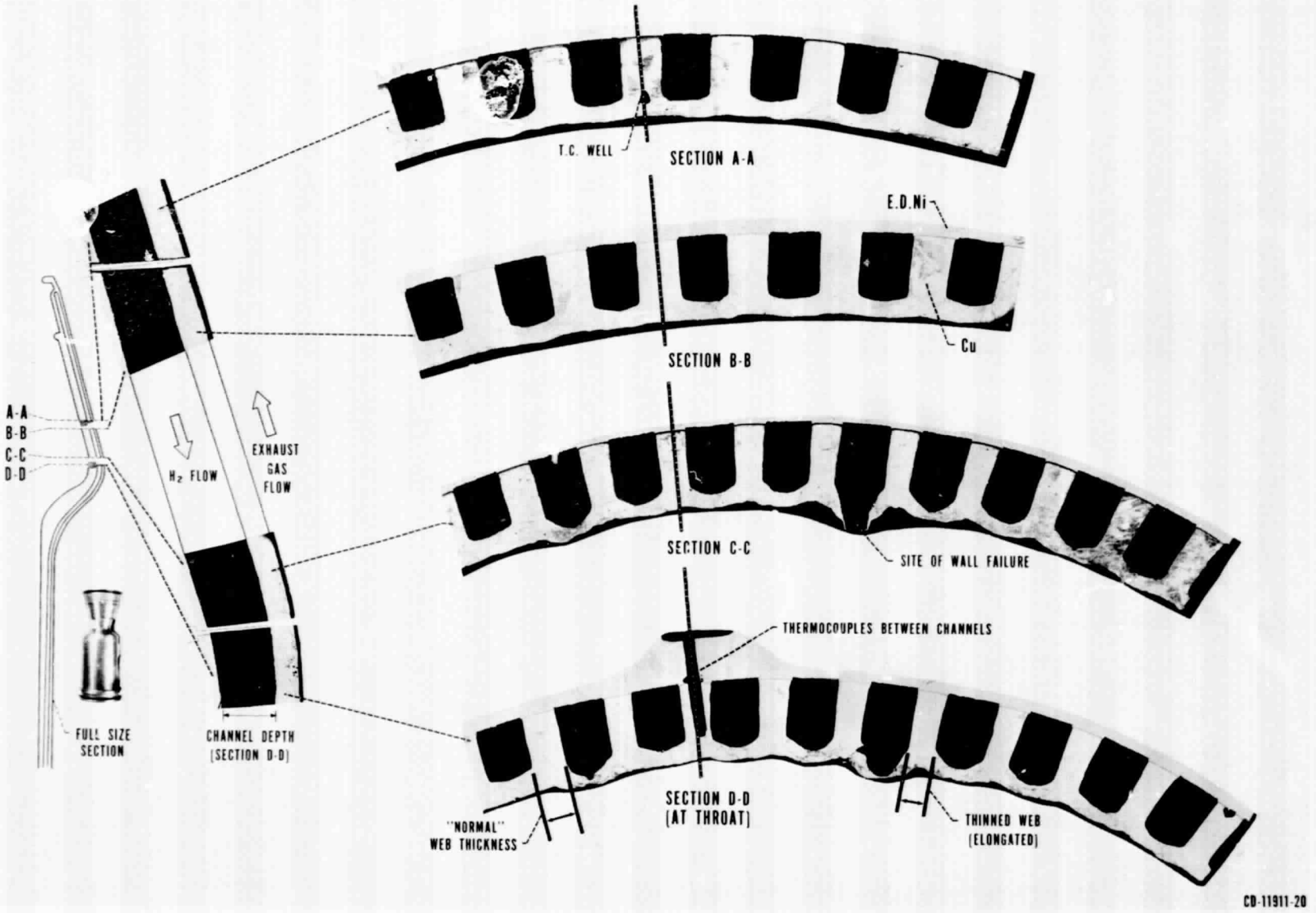

Figure 14. - Deformation of OFHC chamber (Sections of chamber S/N 40).

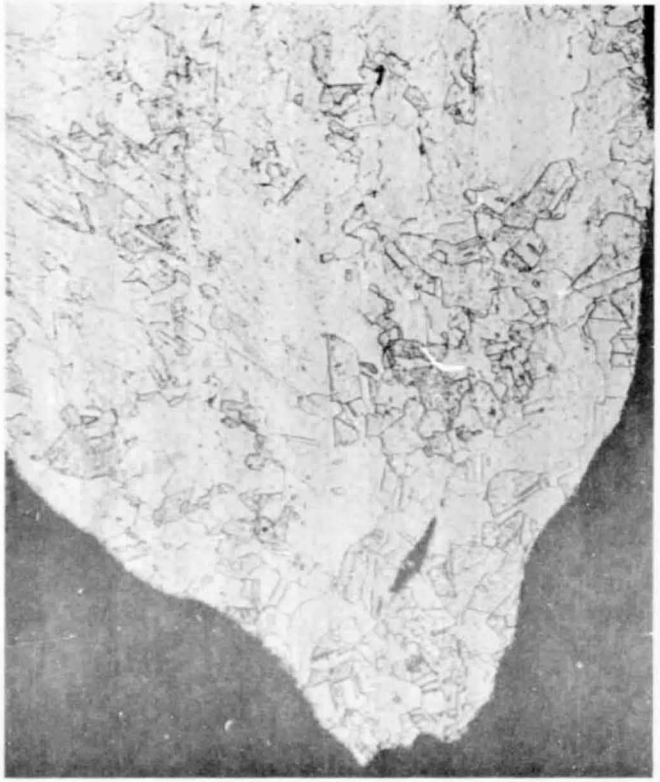

Figure 15. - Enlarged (X150) cross-sectional photograph of a failure site with an OFHC copper chamber liner.

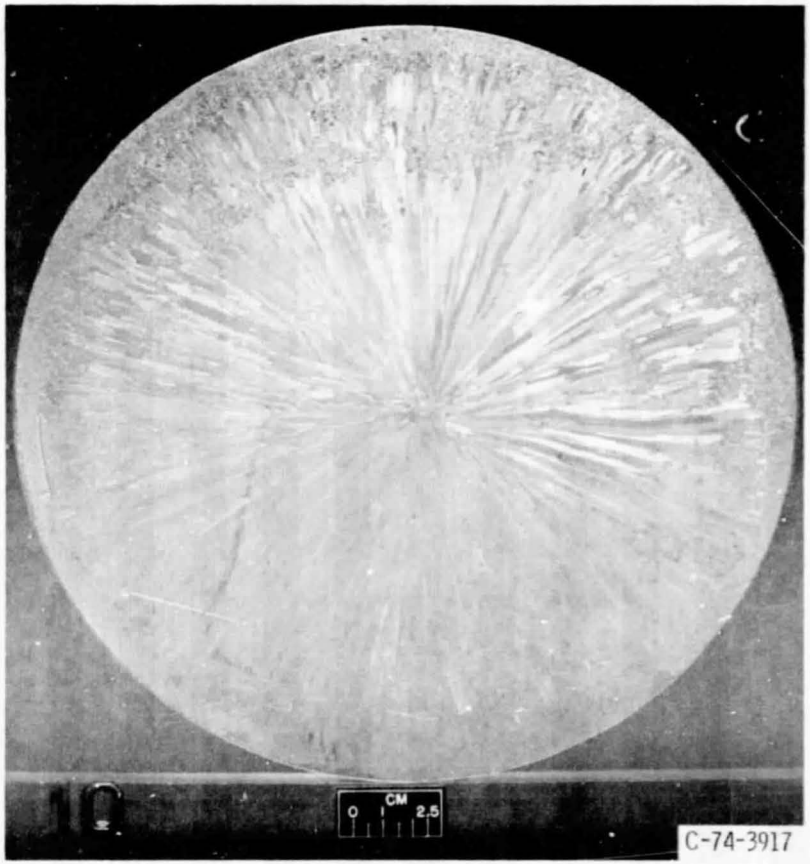

Figure 16. - OFHC copper billet used to fabricate chamber S/N 10.

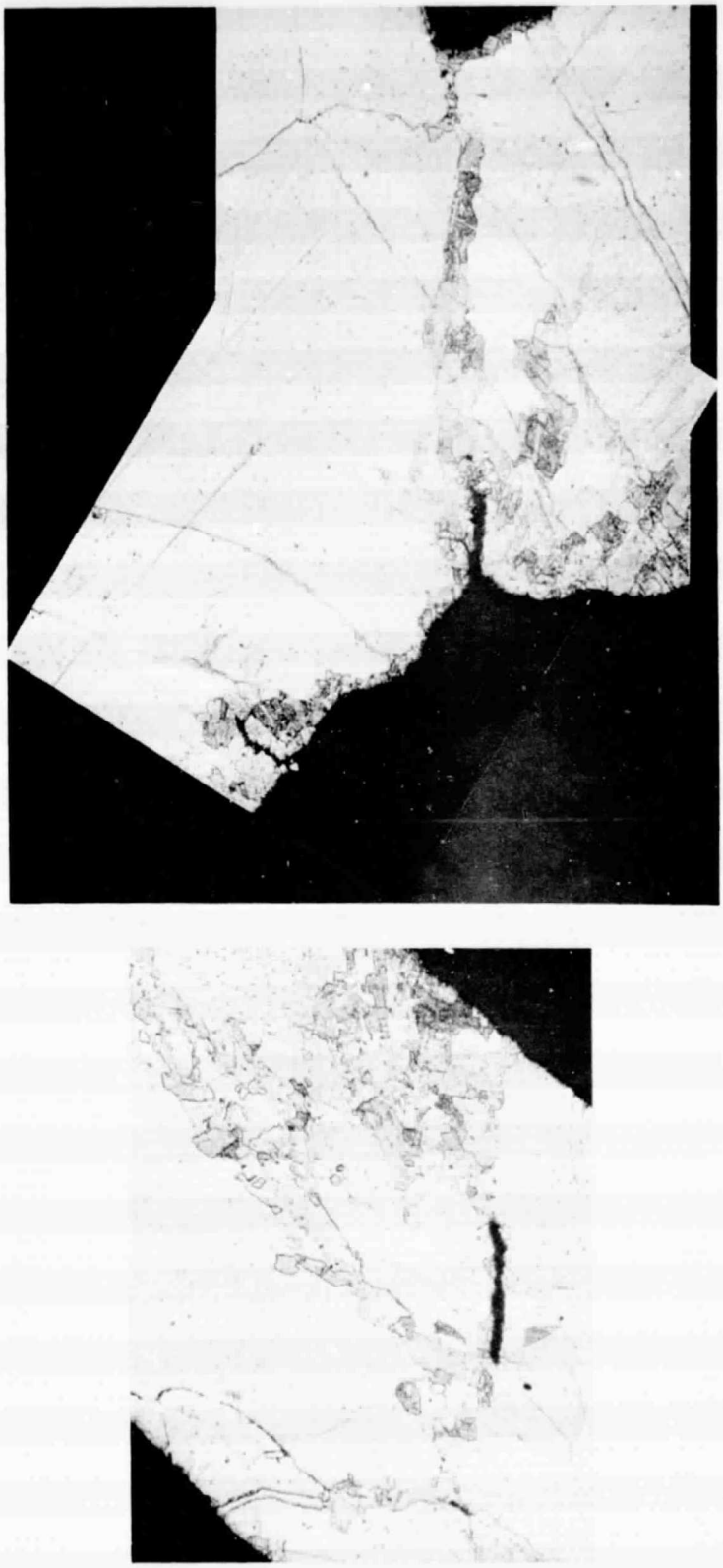

Figure 17. - Enlarged (X150) cross-sectional photograph showing recrystallization and cracking of grain boundaries with an OFHC copper chamber.

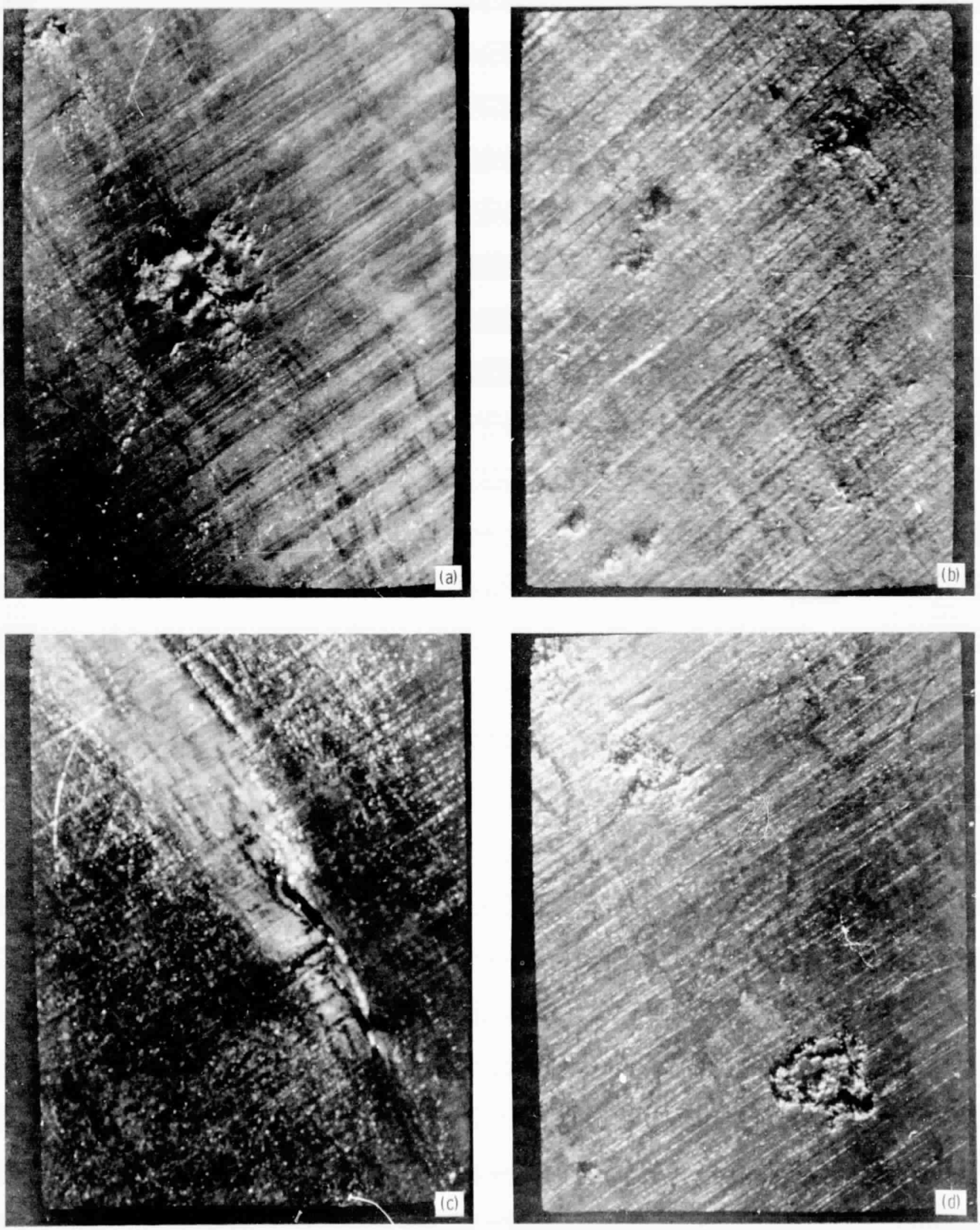

Figure 18. - Enlarged (X15) photographs of surface pits.

Figure 19. - Scanning electron microscope photograph of fracture surface. Chamber S/N 120.